

Nonperturbative approach to photoemission by direct simulation of photocurrents

H. Husser,^{*} J. van Heys, and E. Pehlke*Institut für Theoretische Physik und Astrophysik, Christian-Albrechts-Universität Kiel, DE-24098 Kiel, Germany*

(Received 15 August 2011; revised manuscript received 23 November 2011; published 21 December 2011)

A procedure is presented for the *ab initio* calculation of the angle- and energy-resolved photocurrents emitted from an atom, molecule, cluster, or solid surface excited by a fs-laser pulse. The approach does not rely on perturbation theory. Instead, it is based on the direct simulation of the photoemission process in the time-and-space domain. Hence, though the focus of the present work is on single-photon photoemission from the Si(001) surface which is presented as a test case, we emphasize that the simulation inherently includes two- and multiphoton photoemission currents. The system is assumed to be initially in its electronic ground state. Its electronic structure is calculated within density functional theory using supercells and a slab geometry. The time evolution of the system is obtained by the integration of the time-dependent Kohn-Sham equations. In case of photoemission from solid surfaces discussed in this paper, the inelastic scattering of the photoelectrons is roughly accounted for by an absorptive gauge-invariant optical potential, which is acting on the excited-state admixtures of the time-dependent single-particle wave functions only. Due to the omission of the inelastically scattered electrons from the calculated charge density, the effective potential cannot be updated any longer and has to be kept frozen during the simulation. Technically, the decoupling of the slabs is achieved by an absorbing potential in the vacuum region. The angle- and energy-resolved photoemission spectrum is obtained from the Fourier transform of the time-dependent single-particle wave functions. Photoemission spectra for the Si(001) surface are compared to experimental data from the literature.

DOI: [10.1103/PhysRevB.84.235135](https://doi.org/10.1103/PhysRevB.84.235135)

PACS number(s): 79.60.Bm, 73.20.At

I. INTRODUCTION

Photoemission has developed into a highly sophisticated tool to obtain detailed information about the electronic structure of solids, clusters, and molecules.¹ Angular resolved ultraviolet photoemission spectroscopy (ARUPS) is applied to solids in order to map the electronic bulk band structure of the occupied states and to determine the \mathbf{k}_{\parallel} dispersion of the eigenenergies of the surface states.¹⁻⁴ In addition, spectral line shapes provide information about the lifetime of excitations of the electronic system and many-body effects contained in the spectral function.^{5,6} In the cases discussed above the electron emission occurs in response to a single-photon absorption event; thus, the process is referred to as one-photon photoemission (1PPE). The unoccupied states below the vacuum level that are not accessible by 1PPE can be probed by inverse photoemission.⁷ On the other hand, with two-photon photoemission (2PPE) at the same time occupied initial and unoccupied intermediate states are probed, which can be disentangled by the different dispersion of peak position with photon energy $\hbar\omega$.⁸ Moreover, 2PPE pump-probe spectroscopy makes it possible to observe dynamical processes directly on the fs time scale.^{9,10} Specifically, with respect to 2PPE from the Si(001) surface, we refer to Refs. 11–15. Beyond this, there is great interest in highly nonlinear effects occurring in strong laser fields such as multiphoton ionization (MPI), above-threshold ionization (ATI), and high harmonic generation (HHG).¹⁶⁻²⁰

The prevailing theoretical interpretation of 1PPE spectra within the single-particle approach is based on the Fermi's golden rule type of equation for the spectrally resolved photocurrent,^{1,21-23}

$$j \sim v_e \sum_i^{\text{occ}} |\langle f | \mathbf{A} \cdot \hat{\mathbf{p}} + \hat{\mathbf{p}} \cdot \mathbf{A} | i \rangle|^2 \delta(\varepsilon_f - \varepsilon_i - \hbar\omega_p). \quad (1)$$

Here v_e denotes the velocity of the photoelectron, \mathbf{A} the vector potential of the incident light wave, and $|i\rangle$ and $|f\rangle$ the initial and final states with energies ε_i and ε_f , respectively. A prefactor containing the distance between specimen and detector R and the photon energy $\hbar\omega_p$ is absorbed into the proportionality factor.

Compared to this rather compact formula for the 1PPE spectra, the perturbation series expansion for the 2PPE spectra with respect to the vector potential results in a more complicated form with a summation over all possible intermediate states.²⁴ In order to calculate higher-order photoemission currents including and beyond 2PPE, a *nonperturbative* approach is therefore clearly desirable. In this paper we present such a nonperturbative approach to photoemission. Conceptually, it is based on previous work in which we have simulated the Si(001) surface exposed to a fs-laser pulse by *ab initio* molecular dynamics based on time-dependent density functional theory (TDDFT).²⁵ While the focus of that simulation was on electron-hole pair excitations and electrons essentially confined to the slab, we present an extension to higher photon energies allowing for electrons to be emitted into the vacuum region. However, we assume here that all atom positions are fixed and we will assume the effective potential to be frozen. The reasons are explained below. We hope that this approach will be useful for the investigation of nonlinear effects in photoemission experiments with strong laser pulses as well as for the investigation of coherence effects in pump-probe experiments with very short pulse lengths.

In an early work paving the way for a nonperturbative treatment of laser-matter interaction, the time-dependent one-electron Schrödinger equation (TDSE) has been integrated by Kulanter²⁶ to study MPI of a hydrogen atom. The solution of the full TDSE for a helium atom was performed by Parker *et al.* in the mid-1990s.²⁷ For heavier atoms and molecules, however,

the numerical effort becomes too demanding. Therefore, electron correlation effects, in particular during the process of nonsequential ionization,²⁸ have mostly been extracted from full TDSE integrations of one-dimensional models for the two-electron systems He (Refs. 29–34) and H₂ (Refs. 35 and 36), respectively. One line of approximate approaches encompasses time-dependent Hartree-Fock (TDHF)³⁷ together with its enhancements to time-dependent unrestricted or extended Hartree-Fock (TDUHF, TDEHF)^{38,39} as well as multiconfigurational time-dependent Hartree-Fock (MCTDHF), at present applicable to systems with up to about ten electrons.^{40,41} However, at the moment, TDDFT seems to be the only viable approach for large systems. A comprehensive overview of TDDFT simulations for atoms, molecules, and clusters in strong laser fields can be found in Part V of the book by Marques *et al.*⁴² In particular, we refer to the work cited there by Ullrich *et al.*,^{43–45} by Bauer and Ceccherini,⁴⁶ and by Tong and Chu^{47,48} for Ne and other noble-gas atoms, further the considerations concerning the kinetic-energy spectra of photoemitted electrons within TDDFT by Vényard *et al.*⁴⁹ Diatomic or linear molecules in strong laser fields have been studied by several authors,^{50–52} while R. Baer *et al.* have considered a benzene molecule exposed to circularly polarized light.⁵³ For the investigation of metal clusters within TDDFT we refer to Refs. 54–57 and in particular to the calculation of photoelectron spectra from Na and K clusters by Pohl *et al.*^{58–60} A review on laser-excited cluster dynamics can be found in Refs. 61 and 62. The nonequilibrium Green's function (NEGF) technique, on the other hand, constitutes a description of the time dependence of the quantum system based on many-particle theory.^{63–66} Comparison to TDDFT calculations can yield the opportunity to test the quality of the approximations to the exchange-correlation functional.

In the present paper we describe our approach to the calculation of photoemission spectra for clusters and solid surfaces by direct simulation. The general theory and the necessary approximations are outlined. As a first application, we present normal emission photoemission spectra (IPPE) for Si(001) calculated for fixed atomic positions and frozen effective potential.

II. THEORY

A. Introduction to theory

We consider an atom, molecule, cluster, or solid surface which is exposed to the electromagnetic field of a femtosecond laser pulse. The system is assumed to be initially in its ground state. The evolution of the electronic system is governed by the time-dependent many-particle Schrödinger equation. In principle, also the nuclei will be accelerated due to the forces exerted on them by the light wave as well as the Coulomb interaction with the induced charge density. Even though their motion can be included within the Ehrenfest approximation in the TDDFT molecular dynamics program,²⁵ in the present calculations all nuclear positions will be assumed to be frozen.

From a general theoretical point of view the dynamics of the electrons can be described by time-dependent current density functional theory (TDCDFT). It has been proven by Vignale (Ref. 67; see also Ref. 68 for the original

Ghosh-Dhara theorem) that there exists a noninteracting Kohn-Sham system, which evolves according to a time-dependent vector potential \mathbf{A}_{KS} and scalar potential v_{KS} with the same charge density $n(\mathbf{r}, t)$ and current density $\mathbf{j}(\mathbf{r}, t)$ as the interacting many-particle system (atomic units will be used throughout this paper):

$$i \frac{\partial \psi}{\partial t} = \left\{ \frac{1}{2} \left(\hat{\mathbf{p}} + \frac{1}{c} \mathbf{A}_{\text{KS}} \right)^2 + v_{\text{KS}} \right\} \psi. \quad (2)$$

The initial wave functions $\psi(\mathbf{r}, 0)$ are taken equal to the Kohn-Sham states entering the DFT ground state. This is a generalization of the Runge-Gross theorem⁶⁹ of TDDFT. It lays the grounds for TDCDFT, in which the current density appears as the basic variable. A well-known problem of TDDFT, namely, the ultra-nonlocal dependence of the Kohn-Sham potential on the induced charge density,⁴² can be overcome in TDCDFT. By keeping track of the time-dependent current density one is able to capture the buildup of macroscopic polarizations or global changes in the charge distribution of an extended periodic system.^{70,71} The macroscopic polarization can be incorporated into TDDFT as an independent degree of freedom (see the work by Kootstra *et al.*⁷² and by Bertsch *et al.*⁷³).

For the objective of the present paper, which focuses on technical aspects of the direct simulation of the photoemission process, we go back to TDDFT and assume the very simple adiabatic local density approximation (ALDA) for the time-dependent exchange-correlation potential (and thereby ignore the ultra-nonlocality problem):

$$i \frac{\partial \psi}{\partial t} = \left\{ \frac{1}{2} \left(\hat{\mathbf{p}} + \frac{1}{c} \mathbf{A} \right)^2 + v_{\text{eff}} \right\} \psi, \quad (3)$$

where \mathbf{A} is the vector potential of the external field and v_{eff} the time-dependent effective potential

$$v_{\text{eff}}(\mathbf{r}, t) = v(\mathbf{r}, t) + \int d^3 \mathbf{r}' \frac{n(\mathbf{r}', t)}{|\mathbf{r} - \mathbf{r}'|} + v_{\text{XC}}^{\text{LDA}}(n(\mathbf{r}, t)). \quad (4)$$

This level of theory has been implemented in the TDDFT code.²⁵ It can be applied to simulate photoemission from atoms, molecules, and small clusters, that is, small finite systems.

However, it is well known that in case of solid surfaces bulk contributions to the photoemission spectra sensitively depend on the k_{\perp} -selection rule, and therewith on the finite escape depth of the photoelectrons.^{1,74} Thus, the inelastic scattering of the photoelectrons in the solid has to be accounted for. This can be achieved by including an optical potential¹ that acts on all conduction states, as is explained in detail below. A disadvantage of this approach is that the time evolution is not unitary anymore due to absorption. Hence, the effective potential cannot be updated and has to be kept frozen at its value from the ground-state DFT calculation. Such an approximation is also tacitly assumed in above golden rule formulation of the photocurrent. We emphasize, however, that, in case of atoms, molecules, or small clusters no optical potential has to be used and no such limitation to a frozen effective potential is necessary.

The theory section is organized as follows. In Sec. II B, the equations of motions are detailed. The slab or supercell

geometry of the simulation and the absorbing boundary conditions (decoupling the slabs or supercells) are presented in Sec. II C. In Sec. II D the nonlocal optical potential operator is described. The following Sec. II E is dedicated to the gauge invariance of our approach. The calculation of energy- and angular-resolved photocurrents (i.e., of the photoemission spectra) is, in fact, a nontrivial problem, which is discussed in Sec. II F as well as Secs. II G, II H, and III.

B. Equations of motion

To avoid complications that arise for infinite systems from the neglect of macroscopic polarizations (see, e.g., Refs. 75 and 76), we conceptually start from finite systems, that is, a cluster or molecule, which are exposed to a light pulse. Our objective is to calculate the induced photocurrent. The diameter of the cluster is assumed to be much smaller than the wavelength of the light pulse. Hence, we can apply the dipole approximation and neglect the spatial variation of the electric field \mathbf{E} or the vector potential \mathbf{A} . The vector potential is given by

$$\mathbf{A}(t) = -c \int_{-\infty}^t dt' \mathbf{E}(t'). \quad (5)$$

The Kohn-Sham electronic equations of motion have the form of a Schrödinger equation for a single particle moving under the influence of a time-dependent effective potential,

$$i \frac{\partial \psi(t)}{\partial t} = \hat{H}_{\text{KS}}^{(\mathbf{A})}(t) \psi(t), \quad (6)$$

where the Kohn-Sham Hamiltonian consists of the following terms:

$$\hat{H}_{\text{KS}}^{(\mathbf{A})}(t) = \frac{1}{2} \left(\hat{\mathbf{p}} + \frac{\mathbf{A}(t)}{c} \right)^2 + \hat{V}_{\text{eff,loc}} + \hat{V}_{\text{ps,nl}}^{(\mathbf{A})} + \hat{V}_{\text{opt}}^{(\mathbf{A})}. \quad (7)$$

In general, both the electric field of the laser pulse and the variation of the Coulomb potential due to the induced charge density difference will result in a nonvanishing force acting on the nuclei. The dynamics of the nuclei can approximately be described by solving the Ehrenfest equations of motion.²⁵ In this work, however, for the sake of simplicity, the atomic positions $\mathbf{R}_i(t)$ will be assumed to be frozen. This assumption is justified since the motion of the nuclei occurs on a distinctly longer time scale than the duration of the laser pulse, which is taken to be of the order of 10 fs in the present simulations.^{25,61}

The time-dependent local contribution to the effective potential comprises the local part of the pseudopotential, the Hartree potential of the time-dependent electron density, and the time-dependent exchange-correlation potential,

$$V_{\text{eff,loc}}(\mathbf{r}, t) = V_{\text{ps,loc}}(\mathbf{r}, \{\mathbf{R}_i(t)\}) + V_{\text{H}}(\mathbf{r}, t) + V_{\text{XC}}[n](\mathbf{r}, t). \quad (8)$$

The xc potential is nonlocal and in general depends on the history of $n(\mathbf{r}, t)$.⁷⁷ In the adiabatic approximation $V_{\text{XC}}[n](\mathbf{r}, t)$ is replaced by the instantaneous charge density inserted into the xc potential of static DFT. Furthermore, we apply either a local density (LDA) or semilocal generalized gradient approximation (GGA) to the static v_{XC} . The ALDA is denoted by $V_{\text{XC}}(n(\mathbf{r}, t))$.

In case of solid surfaces it will turn out to be necessary to go back to non-self-consistent calculations. This approach is

quite common in 1PPE theory, which is based on a golden-rule expression for the photoemission matrix elements. In this case, a single active electron is moving in the frozen ground-state effective potential, as derived from the ground-state electron density $n_0(\mathbf{r})$, plus the time-dependent external field,

$$V_{\text{eff,loc}}(\mathbf{r}) = V_{\text{ps,loc}}(\mathbf{r}, \{\mathbf{R}_i\}) + V_{\text{H}}(\mathbf{r}) + V_{\text{XC}}(n_0(\mathbf{r})). \quad (9)$$

The theory below encompasses both situations, that is, both self-consistent calculations for molecules and clusters and non-self-consistent calculations for solid surfaces.

For the nonlocal part of the pseudopotentials we use the fully separable form established by Kleinman and Bylander,^{78–82} now with a time-dependent gauge factor⁸³ (as discussed below in Sec. II E),

$$V_{\text{ps,nl}}^{(\mathbf{A})}(\mathbf{r}, \mathbf{r}', t) = \sum_i \sum_{(l,m)} \epsilon_l \phi_{i;(l,m)}^{\text{KB}}(\mathbf{r}) \phi_{i;(l,m)}^{\text{KB}}(\mathbf{r}')^* e^{-i(\mathbf{r}-\mathbf{r}') \cdot \mathbf{A}(t)/c}, \quad (10)$$

with $\phi_{i;(l,m)}^{\text{KB}}$ and ϵ_l denoting the KB orbitals and KB energies for atom i and angular momenta (l, m) , respectively.

Usage of pseudopotentials instead of all-electron calculations introduces certain sources of errors. First of all, the polarization of the core electrons is neglected due to the frozen-core approximation, which is an unavoidable prerequisite of any pseudopotential construction. Furthermore, it is known (e.g., from the energy dependence of the logarithmic derivatives of the Kohn-Sham wave functions⁷⁸) that standard pseudopotentials represent the scattering properties of the ions accurately only within the energy range of the occupied states plus some energy interval above the Fermi level, but not necessarily within the energy range of the photoexcited electrons. However, recently Luppi *et al.*⁸⁴ have investigated the influence of the Si pseudopotential on excited-state properties, like the dielectric function of bulk Si. They conclude that the pseudopotential approximation can be applied to excited state calculations even several tens of eV above the Fermi level.

The nonlocal optical potential operator $\hat{V}_{\text{opt}}^{(\mathbf{A})}$ introduced for the case of photoemission from solid-state surfaces is discussed below in Sec. II D.

Within the dipole approximation, the Hamiltonian for solid surfaces in Eq. (7) is invariant with respect to translations by lattice vectors parallel to the surface. Therefore, the components of the Bloch vector parallel to the surface are constants of motion, and the following ansatz for the time-dependent Kohn-Sham wave function is justified:

$$\psi_{\mathbf{k}_{\parallel},j}(\mathbf{r}, t) = w_{\mathbf{k}_{\parallel},j}(\mathbf{r}, t) e^{i\mathbf{k}_{\parallel} \cdot \mathbf{r}}. \quad (11)$$

Here $w_{\mathbf{k}_{\parallel},j}(\mathbf{r}, t)$ has the translational periodicity of the lattice. This observation allows us to expand the time-dependent Kohn-Sham wave functions with respect to plane waves in the usual form known from static DFT.

C. Simulation geometry with absorbing boundaries

For the simulations we use a repeated-slab geometry, as is usually employed for calculations of solid surfaces, adsorption and chemical reactions on surfaces, etc., within DFT.⁸⁵ With regard to ground-state electronic properties, the slabs are decoupled by a sufficiently thick vacuum layer. A periodically

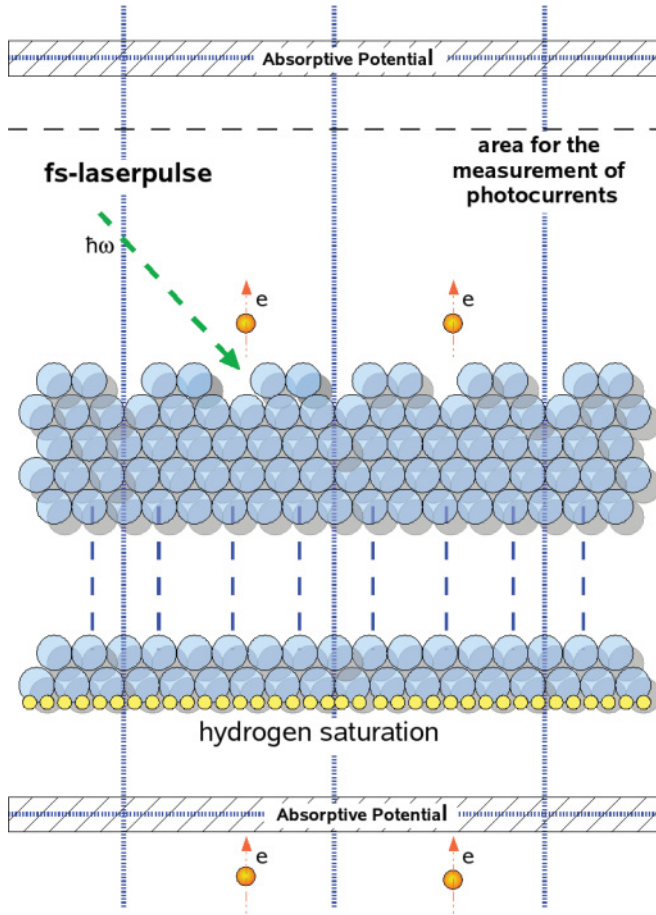


FIG. 1. (Color online) Schematic side view of the slab geometry for the simulation of photoemission from crystal surfaces. The dotted blue lines mark the boundaries of the periodically repeated supercells. The dangling bonds at the bottom surface are saturated by hydrogen atoms (small filled circles). Photocurrents are prevented from impinging on neighboring surfaces by an absorptive potential. The region of nonvanishing absorptive potential within the vacuum region between the slabs is hatched. The photocurrents are measured at the plane indicated by the dashed line.

repeated supercell is used to describe the periodically repeated crystal slabs and the vacuum region (see Fig. 1).

A time-dependent homogeneous electric field normal to the surface can be applied to the slab in a similar way as in case of a static electric field, see, for example, the work by J. Neugebauer and M. Scheffler.⁸⁶ The linear scalar potential corresponding to the homogeneous time-dependent electric field $E(t)\mathbf{e}_z$ within the range of the slab,

$$\Phi(z,t) = -zE(t), \quad (12)$$

is forced to be periodic by introducing a potential jump in the middle of the vacuum region. Otherwise a vector potential \mathbf{A} can be used, together with a vanishing scalar potential Φ , in order to describe the exciting field.

A further problem arises when the photon field leads to photoelectric emission of electrons. In this case, without further precautions, the photocurrent emitted by a crystal slab would impinge on the neighboring slab and would partially penetrate the slab or be reflected. To avoid this, we add a

complex absorptive potential (i.e., a complex potential with a negative imaginary part) $v_{\text{abs}}(z)$, which is nonvanishing only within a thin slab within the vacuum region (for details we refer to Sec. III C). In the practical calculations including such a potential it has turned out to be advantageous to use a nonlocal potential \hat{v}_{abs} instead of the local potential, which acts on the excited-state part of the Kohn-Sham wave functions only, but not on the tails of the single particle orbitals of the Kohn-Sham ground state. In this way artificial damping of ground-state wave functions is avoided. Let \hat{P}_V be the projector onto the Kohn-Sham ground state, then we use the nonlocal absorptive potential

$$\hat{v}_{\text{abs}}^{(\mathbf{A})} = (\hat{1} - \hat{P}_V^{(\mathbf{A})})v_{\text{abs}}(z)(\hat{1} - \hat{P}_V^{(\mathbf{A})}). \quad (13)$$

Here the superscript indicates that in case of a vector potential $\mathbf{A} \neq 0$ the projector onto the electronic valence states $\hat{P}_V^{(\mathbf{A})}$ has to be augmented by a gauge factor as described in the following section.

D. Optical potential

For the description of the photoemission at solid surfaces it is essential to account for the finite mean free path of the photoelectrons in the solid. It is the finite escape depth of the photoelectrons that makes UV photoemission surface sensitive. Moreover, it explains the occurrence of the broadened k_{\perp} selection rule. A very rough approach commonly used in photoemission theory is to consider the attenuation of the elastically scattered component of the wave function, but to disregard the inelastically scattered electrons. This can be achieved by introducing a z -dependent optical potential, which is nonvanishing within the bulk. This optical potential results in a damping of the excited wave functions within the range of the slab. Technically, we restrict the damping to the excited-state admixtures of the time-dependent Kohn-Sham wave functions by projection onto the conduction bands. The optical potential v_{opt} is set constant inside the crystal, falling off to zero in the transition region to the vacuum. The spatial decay of $v_{\text{opt}}(z)$ has been chosen proportional to the ground-state electron density profile $\bar{n}(z)$ averaged in the directions parallel to the surface. The constant value of the optical potential within the crystal is taken equal to the imaginary part of the self-energy (of an electron at an average excitation level) as obtainable from many-particle calculations.^{87–90} Neither the energy nor the wave-vector dependence of the self-energy are accounted for.

Altogether, our optical-potential operator reads

$$\hat{V}_{\text{opt}}^{(\mathbf{A})} = (\hat{1} - \hat{P}_V^{(\mathbf{A})})v_{\text{opt}}(z)(\hat{1} - \hat{P}_V^{(\mathbf{A})}). \quad (14)$$

This equation is formally identical to Eq. (13). As above, $\hat{P}_V^{(\mathbf{A})}$ denotes the valence-band projector. For a periodically repeated supercell its kernel is given by

$$P_V^{(\mathbf{A})}(\mathbf{r}, \mathbf{r}') = \sum_{j(\text{occ})} \int_{\Omega_{\text{BZ}}} \frac{d^3\mathbf{k}}{\Omega_{\text{BZ}}} \varphi_{\mathbf{k},j}(\mathbf{r})\varphi_{\mathbf{k},j}^*(\mathbf{r}')e^{-i(\mathbf{r}-\mathbf{r}')\cdot\mathbf{A}(t)/c}, \quad (15)$$

with the appropriate gauge factor (see Sec. II E) and where the indices \mathbf{k}, j are the three-dimensional Bloch vector and band index of the occupied valence states in the supercell and Ω_{BZ}

denotes the volume of the three-dimensional Brillouin zone of the superlattice.

For the numerical computation of photocurrents from certain initial states the time-development of the Kohn-Sham wave functions has to be calculated only for a small, discrete set of Bloch vectors in the two-dimensional (2D) Brillouin-zone of the crystal slab. We call these wave vectors \mathbf{k}_{\parallel}^0 below. In general, the component of the Bloch vector perpendicular to the layers is set to zero, that is, $\mathbf{k}^0 = (\mathbf{k}_{\parallel}^0, \mathbf{k}_{\perp}^0) = (\mathbf{k}_{\parallel}^0, 0)$. In case of finite systems, $\mathbf{k}^0 = \mathbf{0}$.

The application of $\hat{P}_V^{(A)}$ to such a state $\psi_{\mathbf{k}_{\parallel}^0, j^0}$ yields

$$\begin{aligned} (\hat{P}_V^{(A)} \psi_{\mathbf{k}_{\parallel}^0, j^0})(\mathbf{r}, t) &= \sum_{j(\text{occ})} \int_{\Omega_{\text{BZ}}} \frac{d^3 \mathbf{k}}{\Omega_{\text{BZ}}} u_{\mathbf{k}, j}(\mathbf{r}) \\ &\times e^{i\mathbf{r} \cdot (\mathbf{k} - \mathbf{A}(t)/c)} \int d^3 \mathbf{r}' u_{\mathbf{k}, j}^*(\mathbf{r}') w_{\mathbf{k}_{\parallel}^0, j^0}(\mathbf{r}', t) \\ &\times e^{i\mathbf{r}' \cdot (\mathbf{k}^0 - (\mathbf{k} - \mathbf{A}(t)/c))}, \end{aligned} \quad (16)$$

where we have split the Bloch functions into phase factors and supercell-periodic parts according to

$$\begin{aligned} \varphi_{\mathbf{k}, j}(\mathbf{r}) &= u_{\mathbf{k}, j}(\mathbf{r}) e^{i\mathbf{r} \cdot \mathbf{k}}, \quad \text{and} \\ \psi_{\mathbf{k}_{\parallel}^0, j^0}(\mathbf{r}, t) &= w_{\mathbf{k}_{\parallel}^0, j^0}(\mathbf{r}, t) e^{i\mathbf{r} \cdot \mathbf{k}^0}, \end{aligned} \quad (17)$$

respectively. The integral over \mathbf{r}' produces a factor proportional to $\delta(\mathbf{k}^0 - (\mathbf{k} - \mathbf{A}(t)/c))$; thus, the only nonvanishing contribution comes from $\mathbf{k} = \mathbf{k}^0 + \mathbf{A}(t)/c$, and we obtain

$$\begin{aligned} (\hat{P}_V^{(A)} \psi_{\mathbf{k}_{\parallel}^0, j^0})(\mathbf{r}, t) &= \sum_{j(\text{occ})} u_{\mathbf{k}^0 + \mathbf{A}(t)/c, j}(\mathbf{r}) e^{i\mathbf{r} \cdot \mathbf{k}^0} \\ &\times \int_{\Omega} d^3 \mathbf{r}' u_{\mathbf{k}^0 + \mathbf{A}(t)/c, j}^*(\mathbf{r}') w_{\mathbf{k}_{\parallel}^0, j^0}(\mathbf{r}', t). \end{aligned} \quad (18)$$

The numerical problem with this form is that it effectively introduces time-dependent shifts of the Bloch vectors

$$\mathbf{k}_{\text{eff}}^0(t) := \mathbf{k}^0 + \mathbf{A}(t)/c, \quad (19)$$

thus coupling states at different points in the Brillouin zone to one another (in particular, the time-dependent wave functions at $\bar{\Gamma}$ with $\mathbf{k}^0 = \mathbf{0}$ to stationary states with Bloch vectors $\mathbf{k} \neq \mathbf{0}$).

An approximation is used setting the periodic parts of the Kohn-Sham wave functions constant in the neighborhood of the \mathbf{k} -points \mathbf{k}^0 , which runs up to neglecting time-dependent shift of the Bloch vectors in the periodic part of the wave functions,

$$u_{\mathbf{k}^0 + \mathbf{A}(t)/c, j} \approx u_{\mathbf{k}^0, j}. \quad (20)$$

This leads to the following approximate expression for the projector onto the valence-band states:

$$P_V^{(A)}(\mathbf{r}, \mathbf{r}') \approx \sum_{j(\text{occ})} \sum_{\mathbf{k}_{\parallel}^0} \varphi_{\mathbf{k}_{\parallel}^0, j}(\mathbf{r}) \varphi_{\mathbf{k}_{\parallel}^0, j}^*(\mathbf{r}'). \quad (21)$$

E. Gauge factors and gauge invariance

A spatially periodic Hamiltonian is a prerequisite for a simulation in a repeated slab geometry. As opposed to finite systems, in case of crystal slabs the periodicity of

the Hamiltonian parallel to surface cannot be enforced by a saw-tooth potential. However, in dipole approximation the electric field can be described by a spatially homogeneous time-dependent vector potential according to Eq. (5), thus conserving periodicity of the Hamiltonian in case of extended systems.

The correct gauge factors to be applied to nonlocal potentials in the presence of external electromagnetic fields have been established in the work by Ismail-Beigi, Chang, and Louie⁸³ for the general case. Results for special cases, in particular, first-order treatments, have been derived before (see references cited in Ismail-Beigi⁸³). For the type of nonlocal operators applied here, where nonlocality arises from projections onto certain subspaces of states, the gauge factors can be derived from the gauge transformations of the wave functions involved. For the particular form of the gauge factors we refer the reader to Eqs. (10) and (15).

In order to shed some light on the approximation resulting in Eq. (21), we now specialize to the situation of grazing incidence of the light wave, with the electric field vector perpendicular to the crystal surface. In this case, there is a simple alternative to the above description of the light wave by the vector potential \mathbf{A} , that is,

$$\Phi = 0, \quad \mathbf{A}(t) = -c \int_{-\infty}^t dt' \mathbf{E}(t'). \quad (22)$$

Instead, we can set the vector potential equal to zero and use a linear scalar potential,

$$\Phi(\mathbf{r}, t) = -z E_z(t), \quad \mathbf{A} = 0. \quad (23)$$

This describes the excitation field acting on a single slab. To proceed with the numerical calculation we switch over to periodically repeated slabs, which are decoupled by absorber layers in the middle of the vacuum regions as described above. The electrostatic potential is assumed to be saw-tooth shaped and thereby periodic also perpendicular to the surface.

In this gauge the Hamiltonian reads

$$\hat{H}_{\text{KS}}(t) = \frac{1}{2} \hat{\mathbf{p}}^2 - \hat{\Phi}(t) + \hat{V}_{\text{eff,loc}} + \hat{V}_{\text{ps,nl}} + \hat{V}_{\text{opt}}. \quad (24)$$

Here the nonlocal potentials take the same form as in static DFT, that is, without the gauge factor of Eqs. (10) and (15), respectively:

$$V_{\text{ps,nl}}(\mathbf{r}, \mathbf{r}', t) = \sum_i \sum_{l,m} \epsilon_l \phi_{i;(l,m)}^{\text{KB}}(\mathbf{r}) \phi_{i;(l,m)}^{\text{KB}}(\mathbf{r}')^* \quad (25)$$

and

$$P_V(\mathbf{r}, \mathbf{r}') = \sum_{j(\text{occ})} \int_{\Omega_{\text{BZ}}^{2\text{D}}} \frac{d^2 \mathbf{k}_{\parallel}}{\Omega_{\text{BZ}}^{2\text{D}}} \varphi_{\mathbf{k}_{\parallel}, j}(\mathbf{r}) \varphi_{\mathbf{k}_{\parallel}, j}^*(\mathbf{r}'). \quad (26)$$

The effect of approximating the projectors onto the valence-band states by Eq. (21) is shown in Fig. 2. We find that the relative intensities of the peaks in the photoemission spectra are affected; however, the variation does not exceed 20%.

F. Calculation of photocurrents

To derive the photoemission spectra from the simulation, the photocurrents in the vacuum region are calculated from

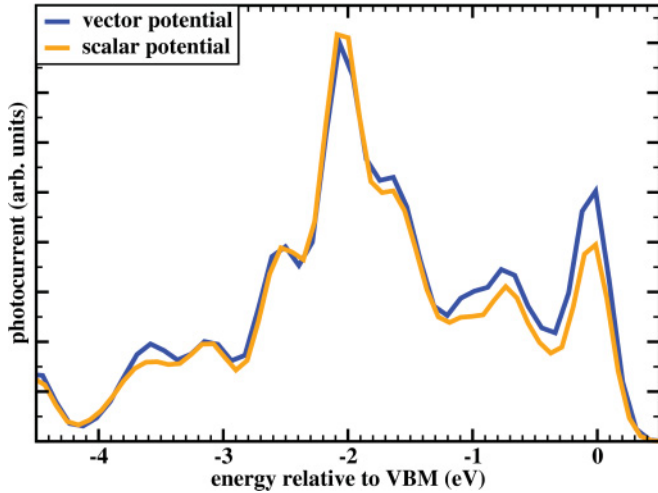


FIG. 2. (Color online) The effect of neglecting the gauge factors in the nonlocal valence-band projectors. The photoemission spectra were calculated using different descriptions of the external field. Blue (or dark gray) line, vector potential according to Eq. (22) and with the approximation (21) for $\hat{P}_V^{(A)}$. The Kleinman-Bylander potential is used in the form of Eq. (10). Orange (or light gray) line, saw-tooth-shaped scalar potential according to (23)–(26). Further parameters of the light pulse: pulse width, $\Delta t_p = 5.0$ fs; frequency, $\hbar\omega_p = 21.2$ eV; maximum field strength, $E_{\max} = 0.0025$ H/ a_0 ; electric field vector oriented normal to the surface.

the time-dependent Kohn-Sham wave functions. We use the simple expression

$$\mathbf{j}_{\mathbf{k}_{\parallel},j}(\mathbf{r},t) = \text{Im}\{\psi_{\mathbf{k}_{\parallel},j}^*(\mathbf{r},t)\nabla\psi_{\mathbf{k}_{\parallel},j}(\mathbf{r},t)\}. \quad (27)$$

We point out that a rigorous treatment of the current densities requires TDCDFT. Furthermore, Eq. (27) only holds in case of vanishing vector potential $\mathbf{A}(\mathbf{r},t)$. We assume that the excitation is due to a laser pulse that is limited to a certain time interval. Thus, Eq. (27) can be applied to calculate the photocurrent after a sufficiently long time, when the vector potential of the laser pulse is negligible. This is in agreement with the experimental setups, where the detector measuring the photoemission spectra is positioned far away from the surface, that is, in a region of vanishing electromagnetic field of the incident light wave.

The problems arising from the limited width of the vacuum region in the simulation can be overcome by transforming the Kohn-Sham wave functions to the Kramers-Henneberger frame (see Refs. 91–95). For the Fourier components, this reads

$$\psi_{\mathbf{k}_{\parallel},j}^{(\text{KH})}(\mathbf{G},t) := \hat{U}\psi_{\mathbf{k}_{\parallel},j}(\mathbf{G},t), \quad (28)$$

with the unitary transformation

$$\hat{U} = e^{i\int_{-\infty}^t dt'((\mathbf{k}_{\parallel}+\mathbf{G})\cdot\mathbf{A}(t')/c) + \frac{1}{2}(\mathbf{A}(t')/c)^2}. \quad (29)$$

In this frame of reference the Hamiltonian takes the form

$$\hat{H}^{(\text{KH})}(t) = \frac{1}{2}\hat{\mathbf{p}}^2 + \hat{V}_{\text{loc}}(\mathbf{r}(t)) + \hat{V}_{\text{nl}}(\mathbf{r}(t),\mathbf{r}'(t)), \quad (30)$$

with

$$\mathbf{r}(t) = \mathbf{r} + \frac{1}{c}\int_{-\infty}^t dt'\mathbf{A}(t'). \quad (31)$$

The Kramers-Henneberger frame is the rest frame of the classical electron moving back and forth under the influence of the external electromagnetic field. In this frame of reference the external electromagnetic field vanishes whereas the ions oscillate (in the present simulations the maximum excursion during excitation remains below $0.025a_0$). Hence, in the vacuum region the perturbation vanishes altogether. Photocurrents and photoemission spectra derived formally from $\psi_{\mathbf{k}_{\parallel},j}^{(\text{KH})}$ do not change in the vacuum region outside the slab. Thus, the currents can be calculated at a z coordinate rather close to the surface. As pointed out above, the laser intensity has become zero when the electrons reach the detector far away from the surface. At that time, $\psi_{\mathbf{k}_{\parallel},j}^{(\text{KH})}$ and $\psi_{\mathbf{k}_{\parallel},j}$ coincide apart from an irrelevant phase factor and an irrelevant spatial shift and yield the same photocurrent.

The total current density at a coordinate z outside the sample is given by summing up the contributions of all initially occupied states,

$$\begin{aligned} \mathbf{j}(\mathbf{r},t) &= \sum_j \int_{\Omega_{\text{BZ}}^{2\text{D}}} \frac{d^2\mathbf{k}_{\parallel}}{\Omega_{\text{BZ}}^{2\text{D}}} 2f_{\text{F}}\left(\frac{\epsilon_j^0(\mathbf{k}_{\parallel}) - \mu}{k_{\text{B}}T}\right) \mathbf{j}_{\mathbf{k}_{\parallel},j}(\mathbf{r},t) \\ &= \sum_j \int_{\Omega_{\text{BZ}}^{2\text{D}}} \frac{d^2\mathbf{k}_{\parallel}}{\Omega_{\text{BZ}}^{2\text{D}}} 2f_{\text{F}}\left(\frac{\epsilon_j^0(\mathbf{k}_{\parallel}) - \mu}{k_{\text{B}}T}\right) \\ &\quad \times \text{Im}\{\psi_{\mathbf{k}_{\parallel},j}^{(\text{KH})*}(\mathbf{r}_{\parallel},z,t)\nabla\psi_{\mathbf{k}_{\parallel},j}^{(\text{KH})}(\mathbf{r}_{\parallel},z,t)\}. \end{aligned} \quad (32)$$

The factor of two accounts for spin degeneracy. Extension to a spin-polarized simulation is straightforward. The integral over \mathbf{k}_{\parallel} extends over the surface Brillouin zone with area $\Omega_{\text{BZ}}^{2\text{D}}$. The sum over j extends over all bands. The contributions from all at least partially occupied bands are considered. f_{F} is the Fermi distribution. It describes the occupation numbers of the ground-state wave functions with Kohn-Sham eigenenergies $\epsilon_j^0(\mathbf{k}_{\parallel})$. For $T \rightarrow 0$, the Fermi occupation probability converges toward a step function selecting the lowest-energy Kohn-Sham eigenstates. The ground-state wave functions are assumed to be taken as initial condition before the laser excitation.

To introduce a spectral and an angular resolution, the action of the detector on the wave functions is described by the application of appropriate projection operators to the wave functions. This is detailed in the following sections. After projection, the wave functions are inserted into Eq. (32) to finally obtain the photoemission spectra.

G. An energy filter for spectral resolution

As we deal with a repeated-slab geometry, the final states of the photoemission process, which are unbound, strongly depend on the vacuum thickness or, equivalently, the overall width of the supercell in the direction perpendicular to the surface. Furthermore, as we apply an absorptive potential, the Hamiltonian would not be Hermitian anymore. For this reason we cannot simply project the time-dependent Kohn-Sham wave functions onto high-energy eigenstates. Instead, we have to resort to a different approach making use of the entire time evolution of the wave functions.

In the following we use a mixed representation of the wave functions, that is, a plane-wave expansion for the two

directions parallel to the surface and a real-space representation for the direction perpendicular to the surface:

$$\psi_{\mathbf{k}_{\parallel},j}^{(\text{KH})}(\mathbf{r},t) = \sum_{\mathbf{G}_{\parallel}} \psi_{\mathbf{k}_{\parallel},j}^{(\text{KH})}(z, \mathbf{G}_{\parallel}, t) \frac{e^{i(\mathbf{k}_{\parallel} + \mathbf{G}_{\parallel}) \cdot \mathbf{r}_{\parallel}}}{\sqrt{\Omega_{2D}}}. \quad (33)$$

Here Ω_{2D} is the area of the surface supercell. The sum extends over all vectors of the 2D-reciprocal lattice. In the numerical simulations the summation is restricted to all 2D-reciprocal lattice vectors up to a certain cutoff energy.

The energy-dependent detection probability of the energy-analyzer is described by a Gaussian function F^2 :

$$F_{\omega_0, \Delta\omega}^2(\omega) = \frac{1}{\sqrt{2\pi} \Delta\omega} e^{-\frac{(\omega - \omega_0)^2}{2\Delta\omega^2}}, \quad (34)$$

with ω_0 and $\Delta\omega$ being the center and width of the detection probability density, respectively.

The action of the energy-selective detector is approximately described by application of the operator $\hat{P}_{\text{erg}} = F_{\omega_0, \Delta\omega}(H^{\text{KH}})$ to the time-dependent Kohn-Sham wave function $\psi_{\mathbf{k}_{\parallel},j}^{(\text{KH})}(\mathbf{r}, t)$ in the Kramers-Henneberger frame. As $\psi_{\mathbf{k}_{\parallel},j}^{(\text{KH})}(\mathbf{r}, t)$ are solutions to the time-dependent Kohn-Sham equations

$$\hat{H}^{(\text{KH})} \psi_{\mathbf{k}_{\parallel},j}^{(\text{KH})} = i \frac{\partial \psi_{\mathbf{k}_{\parallel},j}^{(\text{KH})}}{\partial t}, \quad (35)$$

we obtain

$$F_{\omega_0, \Delta\omega}(\hat{H}^{(\text{KH})}) \psi_{\mathbf{k}_{\parallel},j}^{(\text{KH})}(\mathbf{r}, t) = F_{\omega_0, \Delta\omega} \left(i \frac{\partial}{\partial t} \right) \psi_{\mathbf{k}_{\parallel},j}^{(\text{KH})}(\mathbf{r}, t). \quad (36)$$

Fourier transform with respect to time t yields

$$\begin{aligned} F_{\omega_0, \Delta\omega}(\hat{H}^{(\text{KH})}) \psi_{\mathbf{k}_{\parallel},j}^{(\text{KH})}(\mathbf{r}, t) \\ = \int_{-\infty}^{\infty} \frac{d\omega}{2\pi} e^{-i\omega t} F_{\omega_0, \Delta\omega}(\omega) \psi_{\mathbf{k}_{\parallel},j}^{(\text{KH})}(\mathbf{r}, \omega). \end{aligned} \quad (37)$$

The plane-wave expansion of the energy-filtered wave function with respect to 2D lattice vectors parallel to the surface takes the form

$$\begin{aligned} F_{\omega_0, \Delta\omega}(\hat{H}^{(\text{KH})}) \psi_{\mathbf{k}_{\parallel},j}^{(\text{KH})}(\mathbf{r}, t) \\ = \sum_{\mathbf{G}_{\parallel}} \int_{-\infty}^{\infty} \frac{d\omega}{2\pi} e^{-i\omega t} F_{\omega_0, \Delta\omega}(\omega) \psi_{\mathbf{k}_{\parallel},j}^{(\text{KH})}(z, \mathbf{G}_{\parallel}, \omega) \\ \times \frac{1}{\sqrt{\Omega_{2D}}} e^{i(\mathbf{k}_{\parallel} + \mathbf{G}_{\parallel}) \cdot \mathbf{r}_{\parallel}}. \end{aligned} \quad (38)$$

H. Angular or momentum resolution

In angle-resolved photoemission experiments the direction of the outgoing photoelectrons is selected by placing the electron detector in the desired direction, as the illuminated sample area is small and the detector is far away from the sample. Detecting direction and the kinetic energy of the photoelectrons make it possible to determine all three components of the momentum vector of the photoemitted electrons outside the sample.

In case of the simulations the geometry is fundamentally different. The illuminated specimen surface extends to infinity. In order to select the direction of the emitted electrons, we make use of the conserved quantities in the vacuum kinetic

energy ω and momentum $\mathbf{k}_{\parallel} + \mathbf{G}_{\parallel}$ parallel to the surface. The emission angles ϑ and φ are derived from

$$\vartheta(\omega, \mathbf{k}_{\parallel} + \mathbf{G}_{\parallel}) = \arcsin \left(\frac{|\mathbf{k}_{\parallel} + \mathbf{G}_{\parallel}|}{\sqrt{2\omega}} \right), \quad (39)$$

$$\varphi(\omega, \mathbf{k}_{\parallel} + \mathbf{G}_{\parallel}) = \arctan \left(\frac{k_y + G_y}{k_x + G_x} \right). \quad (40)$$

The acceptance direction $\hat{\mathbf{n}}$ of the detector is defined by the angles ϑ_0 and φ_0 ,

$$\hat{\mathbf{n}} = \cos \vartheta_0 \hat{\mathbf{e}}_z + \sin \vartheta_0 (\cos \varphi_0 \hat{\mathbf{e}}_x + \sin \varphi_0 \hat{\mathbf{e}}_y). \quad (41)$$

The finite angular resolution of the detector is taken into account by tolerance angles $\Delta\vartheta$ and $\Delta\varphi$. This leads to the characteristic function for a detector in direction $\hat{\mathbf{n}}$,

$$\chi_{\hat{\mathbf{n}}, \Delta\Omega}(\mathbf{k}_{\parallel} + \mathbf{G}_{\parallel}, \omega) := \begin{cases} 1 & \text{if } |\vartheta - \vartheta_0| \leq \Delta\vartheta, \\ & \text{and } |\varphi - \varphi_0| \leq \Delta\varphi, \\ 0 & \text{else.} \end{cases} \quad (42)$$

Thus, we define the action of the operator \hat{P}_{dir} that is selecting the emission direction to the energy-filtered wave function $\hat{P}_{\text{erg}} \psi_{\mathbf{k}_{\parallel},j}^{(\text{KH})}(\mathbf{r}, t)$ [Eq. (38)] as

$$\begin{aligned} \hat{P}_{\text{dir}} \hat{P}_{\text{erg}} \psi_{\mathbf{k}_{\parallel},j}^{(\text{KH})}(\mathbf{r}, t) &= \hat{P}_{\text{dir}} \sum_{\mathbf{G}_{\parallel}} \int_{-\infty}^{\infty} \frac{d\omega}{2\pi} e^{-i\omega t} F_{\omega_0, \Delta\omega}(\omega) \\ &\times \psi_{\mathbf{k}_{\parallel},j}^{(\text{KH})}(z, \mathbf{G}_{\parallel}, \omega) \frac{1}{\sqrt{\Omega_{2D}}} e^{i(\mathbf{k}_{\parallel} + \mathbf{G}_{\parallel}) \cdot \mathbf{r}_{\parallel}} \\ &= \sum_{\mathbf{G}_{\parallel}} \int_{-\infty}^{\infty} \frac{d\omega}{2\pi} e^{-i\omega t} \\ &\times \chi_{\hat{\mathbf{n}}, \Delta\Omega}(\mathbf{k}_{\parallel} + \mathbf{G}_{\parallel}, \omega) F_{\omega_0, \Delta\omega}(\omega) \\ &\times \psi_{\mathbf{k}_{\parallel},j}^{(\text{KH})}(z, \mathbf{G}_{\parallel}, \omega) \frac{e^{i(\mathbf{k}_{\parallel} + \mathbf{G}_{\parallel}) \cdot \mathbf{r}_{\parallel}}}{\sqrt{\Omega_{2D}}}. \end{aligned} \quad (43)$$

In summary, the energy and direction filter operators are defined by multiplication of the Fourier-transformed wave function expansion coefficients $\psi_{\mathbf{k}_{\parallel},j}^{(\text{KH})}(z, \mathbf{G}_{\parallel}, \omega)$ by local resolution functions $F_{\omega_0, \Delta\omega}(\omega)$ and $\chi_{\hat{\mathbf{n}}, \Delta\Omega}(\mathbf{k}_{\parallel} + \mathbf{G}_{\parallel}, \omega)$.

I. Calculation of photoemission spectra

Experimentally, the photoemission spectrum is given by the number of electrons detected at a certain energy ω_0 in a certain direction $\hat{\mathbf{n}}$. In the simulation we assume a laser pulse of finite duration. The electron count rate in the detector, integrated over many pulses, will be proportional to the expectation value of the total photoemitted charge per surface unit cell. The energy and angular resolution of the detector is accounted for by applying the filter operators \hat{P}_{dir} and \hat{P}_{erg} defined in the previous section.

Inserting the filtered wave functions (43) into Eq. (32) for the current density we obtain the following expression for the

energy- and angular-resolved photocurrent density:

$$\begin{aligned} \mathbf{j}_{\hat{\mathbf{n}},\omega_0}(\mathbf{r},t) &= \frac{1}{\Omega_{2D}} \sum_j \int_{\Omega_{BZ}^{2D}} \frac{d^2\mathbf{k}_{\parallel}}{\Omega_{BZ}^{2D}} 2f_F \left(\frac{\epsilon_j^0(\mathbf{k}_{\parallel}) - \mu}{k_B T} \right) \text{Im} \int_{-\infty}^{\infty} \frac{d\omega}{2\pi} \int_{-\infty}^{\infty} \frac{d\omega'}{2\pi} F_{\omega_0,\Delta\omega}^*(\omega') F_{\omega_0,\Delta\omega}(\omega) e^{-i(\omega-\omega')t} \sum_{\mathbf{G}_{\parallel}} \sum_{\mathbf{G}'_{\parallel}} \chi_{\hat{\mathbf{n}},\Delta\Omega}^* \\ &\times (\mathbf{k}_{\parallel} + \mathbf{G}'_{\parallel},\omega') \chi_{\hat{\mathbf{n}},\Delta\Omega}(\mathbf{k}_{\parallel} + \mathbf{G}_{\parallel},\omega) \psi_{\mathbf{k}_{\parallel},j}^{(KH)*}(z,\mathbf{G}'_{\parallel},\omega') \left(i(\mathbf{k}_{\parallel} + \mathbf{G}_{\parallel}) + \hat{\mathbf{e}}_z \frac{\partial}{\partial z} \right) \psi_{\mathbf{k}_{\parallel},j}^{(KH)}(z,\mathbf{G}_{\parallel},\omega) e^{-i(\mathbf{G}_{\parallel}-\mathbf{G}'_{\parallel})\cdot\mathbf{r}_{\parallel}}. \end{aligned} \quad (44)$$

The total photoemitted charge per unit cell as observed in a photoemission experiment is obtained by integrating this current density (44) both over time and over the cross-section of the slab:

$$\Delta q_{\hat{\mathbf{n}},\omega_0} = \int_{\Omega_{2D}} d^2\mathbf{r}_{\parallel} \int_{-\infty}^{\infty} dt \mathbf{j}_{\hat{\mathbf{n}},\omega_0}(\mathbf{r}_{\parallel},z,t) \cdot \hat{\mathbf{e}}_z. \quad (45)$$

The integration over time yields a δ function,

$$\int_{-\infty}^{\infty} dt e^{-i(\omega-\omega')t} = 2\pi \delta(\omega - \omega'), \quad (46)$$

and the integration over the surface unit cell yields

$$\int_{\Omega_{2D}} d^2\mathbf{r}_{\parallel} e^{i(\mathbf{G}_{\parallel}-\mathbf{G}'_{\parallel})\cdot\mathbf{r}_{\parallel}} = \Omega_{2D} \delta_{\mathbf{G}_{\parallel},\mathbf{G}'_{\parallel}}. \quad (47)$$

Thus, the total photoemitted charge simplifies to

$$\begin{aligned} \Delta q_{\hat{\mathbf{n}},\omega_0} &= \sum_j \int_{\Omega_{BZ}^{2D}} \frac{d^2\mathbf{k}_{\parallel}}{\Omega_{BZ}^{2D}} 2f_F \left(\frac{\epsilon_j^0(\mathbf{k}_{\parallel}) - \mu}{k_B T} \right) \\ &\times \int_{-\infty}^{\infty} \frac{d\omega}{2\pi} F_{\omega_0,\Delta\omega}^2(\omega) \sum_{\mathbf{G}_{\parallel}} \chi_{\hat{\mathbf{n}},\Delta\Omega}(\mathbf{k}_{\parallel} + \mathbf{G}_{\parallel},\omega) \\ &\times \text{Im} \left\{ \psi_{\mathbf{k}_{\parallel},j}^{(KH)*}(z,\mathbf{G}_{\parallel},\omega) \frac{\partial}{\partial z} \psi_{\mathbf{k}_{\parallel},j}^{(KH)}(z,\mathbf{G}_{\parallel},\omega) \right\}, \end{aligned} \quad (48)$$

where we have used the identity $\chi^* \chi = |\chi|^2 = \chi$.

Next we specialize to the case of normal emission of the photoelectrons. The angular resolution of the detector is assumed to be such that only the $\mathbf{G}_{\parallel} = 0$ components of the wave functions are detected. Thus, the sum over \mathbf{G}_{\parallel} in Eq. (48) reduces to the term for $\mathbf{G}_{\parallel} = 0$. Furthermore, we assume a semiconducting band structure, or, less restrictively, that all bands entering Eq. (48) are, within the acceptance cone of the detector, either fully occupied, $f_F = 1$, or fully unoccupied, $f_F = 0$. We also neglect the \mathbf{k}_{\parallel} dependence of $\text{Im}\{\psi_j^*(z,\mathbf{k}_{\parallel} + \mathbf{G}_{\parallel},\omega)(\nabla_z \psi_j)(z,\mathbf{k}_{\parallel} + \mathbf{G}_{\parallel},\omega)\}$. In this case, the remaining integral reduces to the ω -dependent area of the Brillouin zone corresponding to the acceptance cone of the detector, $\Delta\Omega_{BZ}^{2D}(\omega) = 2\pi\omega\Delta\vartheta^2$, divided by the area of the 2D Brillouin zone of the supercell Ω_{BZ}^{2D} ,

$$\int \frac{d^2\mathbf{k}_{\parallel}}{\Omega_{BZ}^{2D}} \chi_{\hat{\mathbf{e}}_z,\Delta\Omega}(\mathbf{k}_{\parallel},\omega) = \frac{\Delta\Omega_{BZ}^{2D}(\omega)}{\Omega_{BZ}^{2D}}. \quad (49)$$

In this case the total photoemitted charge can be written as

$$\begin{aligned} \Delta q_{\hat{\mathbf{e}}_z,\omega_0} &= \int_{-\infty}^{\infty} \frac{d\omega}{2\pi} F_{\omega_0,\Delta\omega}^2(\omega) \frac{\Delta\Omega_{BZ}^{2D}(\omega)}{\Omega_{BZ}^{2D}} \\ &\times 2 \sum_{j,\text{occ}} \text{Im} \left\{ \psi_{\mathbf{0},j}^{(KH)*}(z,\mathbf{0},\omega) \frac{\partial}{\partial z} \psi_{\mathbf{0},j}^{(KH)}(z,\mathbf{0},\omega) \right\}. \end{aligned} \quad (50)$$

III. IMPLEMENTATION AND APPLICATION TO ONE-PHOTON PHOTOEMISSION FROM Si(001)

After a brief description of the Si(001) surface reconstruction in Sec. III A, we give some details on the implementation of the photoemission simulation program together with the parameters required for converged spectra in Sec. III B. In Secs. III C and III E, we discuss the absorptive and the optical potential, respectively. The exciting laser pulse is introduced in Sec. III D. In Sec. III F, the dipole selection rules in case of normal emission due to the symmetry of the $p(2 \times 2)$ -reconstructed surface are summarized. In the final Sec. III G we compare—as a test case—simulated 1PPE spectra from this surface to experimental data by Johansson *et al.*⁹⁶ and analyze the photoemission spectra in terms of the initial states that contribute.

A. Surface structure and emission geometry

The surface geometry of Si(001) has been studied intensely both experimentally and theoretically.⁹⁷ The $p(2 \times 2)$ and $c(4 \times 2)$ surface reconstructions are characterized by dimer rows. The Si dimers buckle, and the buckling angle alternates along the dimer rows. The two reconstructions differ only in the relative phase of the dimer buckling in adjacent rows. Figure 3 shows a schematic top view of the $p(2 \times 2)$ reconstruction, which, for the sake of simplicity, has been assumed for all calculations in this work.

On terraces separated by single atomic height steps the orientation of the Si-dimer bond differs by 90° . Nominally flat Si(001) surfaces contain steps. Thus, to compare to experimental photoemission spectra, an incoherent average over the two orientations of dimerization has to be performed. At increased miscut of the order of few degrees along one of the $\langle 110 \rangle$ directions double atomic steps prevail and the vicinal surface becomes single domain.⁹⁸

For the calculation we use a Cartesian coordinate system with x and y axes within the surface plane, and the z axis pointing outward from the Si bulk into the vacuum. The angle of incidence of the laser beam with respect to the surface normal will be denoted by θ . The component of the electric field vector in the plane of the Si surface is oriented either parallel or perpendicular to the dimer bonds. In the final photoemission spectra, both orientations have been averaged over.

The surface electronic structure in the energy gap between the valence and the conduction states in the projected band structure consists of occupied and unoccupied surface states derived from the dangling bonds at the Si-up and Si-down atoms, respectively.^{87,99–102} Due to the (2×2) cell there are

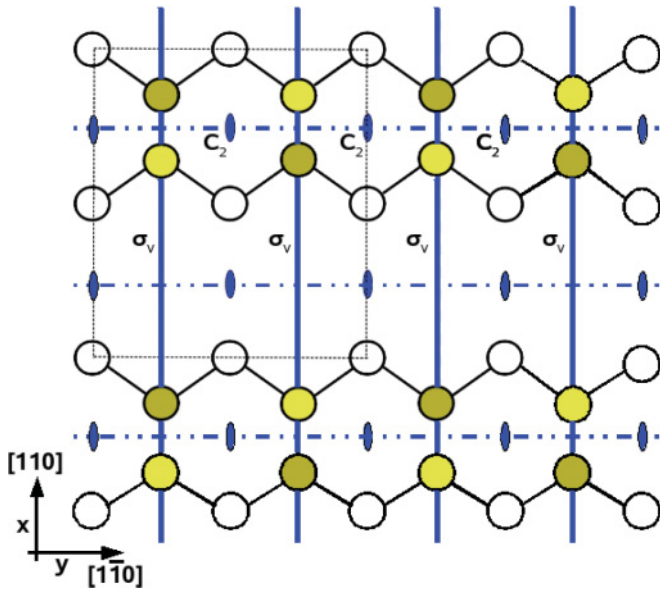


FIG. 3. (Color online) Si(001) surface geometry (top view). Top-layer Si atoms are denoted by shaded circles. Darker shade denotes the atoms of the Si dimer that have relaxed outward toward the vacuum (Si-up atoms). Lighter shade denotes the Si-down dimer atoms, which are closer to the bulk. The thin dashed line frames the $p(2 \times 2)$ surface unit cell. Mirror planes perpendicular to the surface (σ_v) are denoted by solid lines, glide planes by dash-dotted lines. Furthermore, the twofold rotational axes (C_2) are indicated.

two surface bands of each type, which we denote with D_{up} and D'_{up} or D_{down} and D'_{down} .

B. Computational details and convergence parameters of the DFT code

The Si surface is simulated within a slab geometry, with a supercell repeated periodically in the directions parallel as well as perpendicular to the surface. The Si-surface atoms on the bottom side of the slab are saturated with hydrogen atoms. Parameters needed to achieve convergence of Si(001) total energy calculations and calculation of the electronic structure are known.¹⁰¹ However, tightened convergence parameters are needed in some cases in order to simulate the angle- and energy-resolved photoemission spectra.

Particular attention has to be paid to the number of silicon layers in the slab. First, for a meaningful description of photoemission from solid surfaces, the thickness of the slab has to exceed the escape depth of the photoelectrons, preferentially by a factor larger than two. In the calculation, the escape depth is determined by the imaginary part of the optical potential. Second, a satisfactory description of the 1D density of states at a given Bloch vector \mathbf{k}_{\parallel} parallel to the surface is indispensable to obtain reasonably smooth spectra. The number of layers can be thought of to correspond to a certain sampling of k_{\perp} , the component of the Bloch vector perpendicular to the surface. Via the dispersion relation $\varepsilon(\mathbf{k}_{\parallel}, k_{\perp})$ of the electronic bulk states (here only the dependence on k_{\perp} for the direction normal to the surface enters), this translates into a set of discrete eigenenergies, which have to represent the smooth variation of the density of states for the true half-space geometry. We find that, in the

case of Si(001) and for the width of the laser pulses as applied in this work, up to 20–36 layers are required in order to obtain reasonably converged normal emission spectra.

Neighboring Si slabs are separated by a sufficiently thick vacuum region that not only has to electronically decouple the surfaces, but which, moreover, has to accommodate the absorptive potential. The spatial extent of the absorptive potential amounts to order of $10a_0$ (Bohr). In the present calculation the absorber is located close to the center of the vacuum region. The distance between the surface and the absorptive potential has to be sufficiently large, so that the photocurrent can be determined before the photoelectron enters the absorber. Furthermore, in particular in case of low frequency and large electric fields of the incident laser pulse, the oscillations of the Si slab in the Kramers-Henneberger frame have to be accounted for (see Sec. II F). Altogether, in the present calculation a thickness of the vacuum region of about $60a_0$ – $70a_0$ has been used, leaving a gap of about $30a_0$ between the absorptive potential in midvacuum and the surface of the slab. This distance is necessary to decouple the absorptive potential from the valence states of the crystal, which are decaying into the vacuum. We note that, as a consequence of the finite cutoff energy limiting the size of our plane-wave basis set, the residual densities of the valence states at the absorber are distinctly larger than would be expected from the exponential decay of the exact Kohn-Sham states. To further reduce this unwanted absorption, we multiply the optical potential with a projector onto conduction states as described above (see Sec. II C).

Photoexcited electrons propagating toward the bulk may be reflected when reaching the back side of the slab. This artificial reflection, which is due to the finite thickness of the slab, becomes irrelevant for thick slabs due to the damping of the photoelectrons by the optical potential within the slab. This is verified by convergence with respect to the slab thickness.

The ground-state atomic configuration and electronic structure of the surface, which enter the simulation as the starting configuration, have been calculated within density functional theory in LDA for the exchange-correlation energy. To obtain a good representation of the electronic ground-state density and frozen-in effective potential in which the photoelectrons will propagate, a \mathbf{k} -point set with nine special wave vectors in the irreducible part of the Brillouin zone has been chosen. In case of the semiconducting Si(001) surface, an energy cutoff of 10–20 Ry in the plane-wave basis set has turned out to be sufficient.

The ground-state configuration of the Si(001) surface has been relaxed with the code FHI96MD from the Fritz Haber institute in Berlin.¹⁰³ The result serves as the initial condition for the real-time simulation of the excitation process. The time-dependent Kohn-Sham equations have been integrated with a modified predictor-corrector scheme,²⁵ which has been implemented in the FHI96MD code. In the present simulations the ion positions have been kept fixed.

C. Choice of the absorptive potential

The effect of a potential with a negative imaginary part (absorptive potential) is to damp the wave functions exponentially with increasing time. Absorptive potentials have long been

used to provide absorbing boundary conditions, for example, for the simulation of scattering processes and of laser-matter interaction within the time domain (see, e.g., Ref. 104 and several of the works cited in the Introduction; alternatively, a so-called mask function¹⁰⁵ can be applied). Optimization of the potential parameters for this purpose, that is, minimization of the transmission and reflection, has been carried through and discussed by D. Neuhauser and M. Baer.¹⁰⁶ Further results in this field have been obtained in the following by several authors (cf. Refs. 107 and 108 and references therein). In the latter paper by Macías *et al.* an extension to complex potentials was considered.

In the present simulation of the photoemission process in the time domain we use an absorptive potential in order to decouple neighboring crystal slabs. Photoemitted electrons are absorbed in the center of the vacuum region. Our supercell geometry puts a technical limit to a practical thickness of the absorber; we only allow for a thickness of the absorber of about $10a_0$.

While for kinetic energies in the range of UV-photoelectrons the transmission probability can easily be suppressed by choosing a sufficiently large imaginary part of the absorptive potential, the reflection probability tends to rise steeply with decreasing kinetic energy of the electron. We ascribe this to the fact that the absorbing potential begins to vary significantly on the length scale of the de Broglie wavelength of the electron.

Partially, this problem can be overcome by adding a real part to the absorber potential, which is attractive and which, roughly spoken, acts as an accelerator for the incoming electrons before they reach the region of strongly absorbing imaginary part of the potential. In this way, the reflection probability can be significantly reduced for the low-energy electrons. Therefore, we use a complex potential $v_{\text{abs}} = v_r + i v_i$, where both parts satisfy $v_r, v_i \leq 0$. In the simulation a real-space grid is used, with a spacing chosen according to the sampling theorem applied to the plane-wave expansion of the electron density. At a plane-wave cutoff energy of 10 Ry, the spacing amounts to $\approx 0.5a_0$. The absorptive potential has to be specified at the grid points falling within the range of the potential. We have minimized the scattered intensity for given energy ranges of the UV-photoelectrons. We assume a Boltzmann distribution of kinetic energy of the electrons and we take the reflection plus the transmission probability, averaged over this distribution of kinetic energies, as a target function for the optimization process. In view of the practical applicability or transferability (keeping the potentials as simple as possible), only monotonically rising polygons for both real and imaginary part were admitted. Within this class of potentials a reduction of the total scattered intensity (transmission plus reflection) as displayed in Fig. 5 can be achieved. The associated absorber potential is displayed in Fig. 4. This complex absorber potential has been applied throughout for the simulations described in this work.

D. Laser pulse for optical excitation

For the excitation we apply a single coherent laser pulse (typically in the UV region), with photon energies in the range from 10 to about 30 eV.

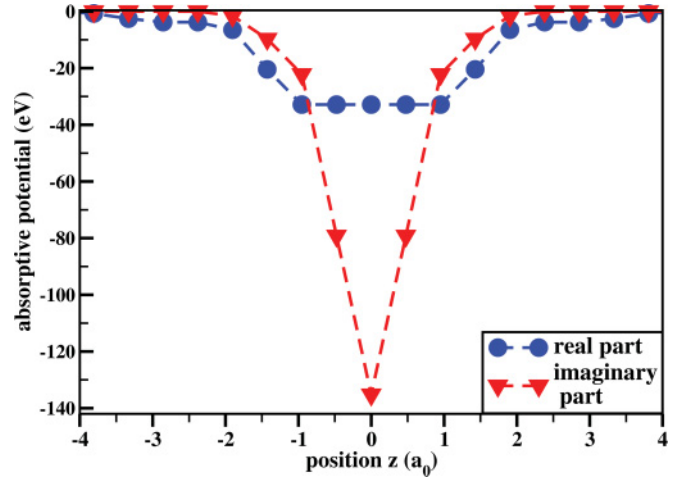


FIG. 4. (Color online) The complex absorptive potential v_{abs} [see Eq. (13)] used for the UV-photoemission calculations. The abscissa gives the position with respect to the center of the vacuum region.

The pulse is given by a Gaussian envelope and a frequency ω_p . In the dipole approximation the spatial variation is dropped. Technically, it is advantageous to limit the support of the laser pulse to a finite time interval $[0, 2t_p]$. Note that, in order to collect all photoemitted electrons, it is necessary to simulate the electron dynamics on a longer time interval $[0, T]$. Altogether, we have

$$\mathbf{E}(\mathbf{r}, t) \equiv \mathbf{E}(t) = \begin{cases} \mathbf{E}_0 \sin(\omega_p t) e^{-\frac{1}{2}(\frac{t-t_p}{\Delta t_p})^2} & \text{for } 0 \leq t \leq 2t_p, \\ 0 & \text{else.} \end{cases} \quad (51)$$

In contrast to attosecond pulses leading to broad band excitations, for an appropriate description of 1PPE light pulses with a duration much larger than the period of the light wave are required. To obtain a sufficiently fine energy resolution $\Delta\omega_p = 1/\Delta t_p$, an accordingly long duration $2t_p$ of the laser

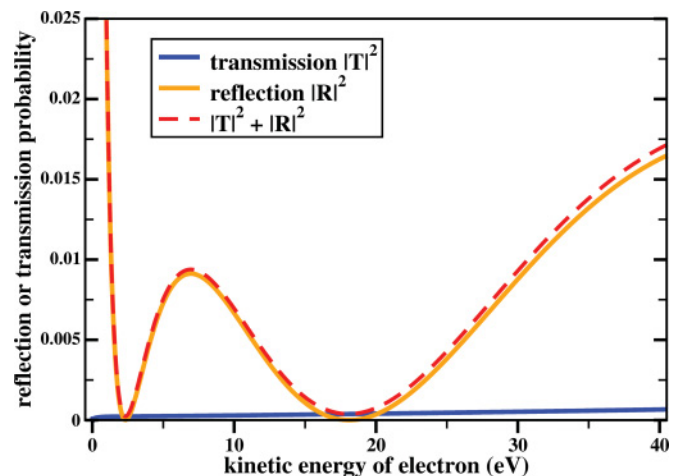


FIG. 5. (Color online) Reflection and transmission probabilities as a function of incident electron energy for the absorptive potential in Fig. 4. Note that the transmission of electrons with kinetic energies in the range of UV-photoemission is negligibly small. Thus, the total transmitted and reflected intensity is dominated by reflection.

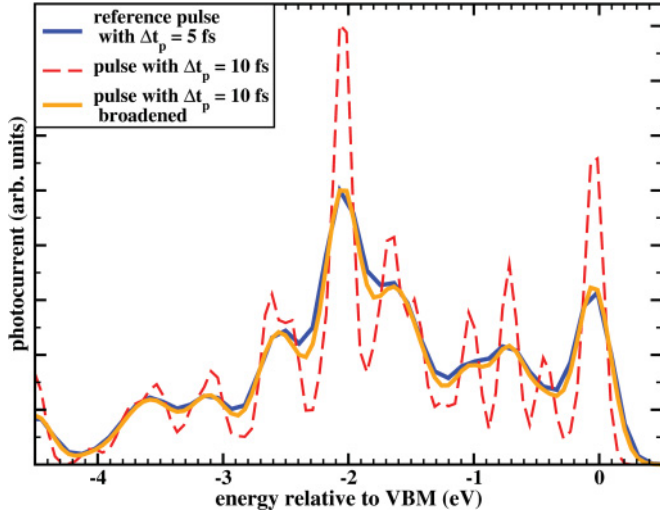


FIG. 6. (Color online) The influence of the pulse duration on the photoemission spectra. The solid blue (dark gray) curve shows the photoemission spectrum for a pulse with a width $\Delta t_p = 5$ fs. This is the pulse width that was used for calculating the photoemission spectra throughout this paper. The dashed red curve was obtained using a pulse with twice this duration, that is, $\Delta t_p = 10$ fs. Subsequent convolution of this spectrum with a Gaussian that corrects for the different spectral widths of the two excitation pulses results in the solid orange (light gray) curve. The photon energy is $\hbar\omega_p = 21.2$ eV and the electric field vector is perpendicular to the surface.

pulse is required. On the other hand, the simulation time is limited due to the computational costs.

In the present work a laser pulse with a width $\Delta t_p = 5$ fs has been chosen, resulting in an energy resolution of $\Delta\omega_p = 130$ meV. Within $2\Delta t_p = 10$ fs there are 20 to 75 cycles of the electrical field. The pulse is switched on at $t = 0$, reaches its maximum at $\approx t_p = 13.7$ fs, and is switched off at $2t_p$, where the electric field amplitude has dropped to $\approx 0.026E_0$. In Fig. 6 the influence of the pulse duration on the photoemission spectra is shown.

In this work, for 1PPE the maximum field strength has been taken as $E_0 \approx 2.5 \times 10^{-3} \text{ H}/a_0 \approx 0.13 \text{ V}/\text{\AA}$, corresponding to a peak intensity of $I \approx 2.2 \times 10^{11} \text{ W}/\text{cm}^2$. We note that the 1PPE part of the spectrum of the photoemitted electrons is expected to scale linearly with the intensity of the light. We have carried through test calculations that confirm this behavior.

E. Estimates for the optical potential

As described above in Sec. II D, the attenuation of the elastic component of the photocurrent due to inelastic scattering processes inside the crystal is accounted for by an optical potential within the slab region acting on the excited part of the electronic wave functions only. In order to preserve the *ab initio* character of the simulations, the values for the optical potential are chosen in accordance with the imaginary part of the quasiparticle self-energy corrections to the Kohn-Sham eigenenergies as calculated within the GW approximation^{109,110} by Fleszar and Hanke,⁹⁰ rather than being estimated from experimental determinations of the electronic mean free path.

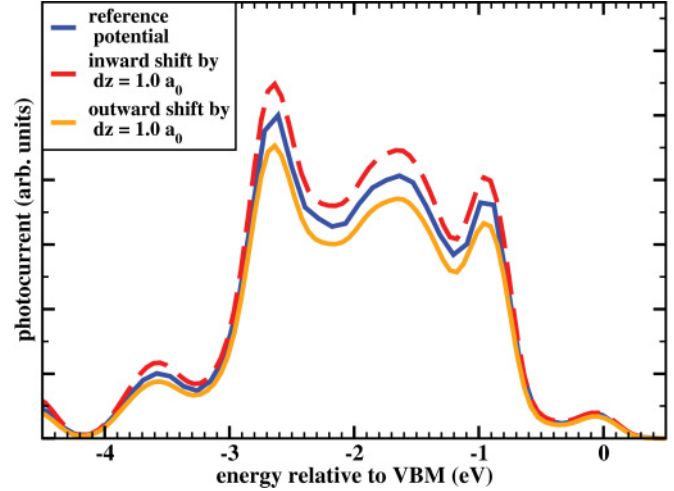


FIG. 7. (Color online) The effect of the spatial extent of the optical potential on the photoemission spectra. The solid blue (dark gray) curve denotes the photoemission spectrum as obtained with the optical potential constructed as described in the text. To obtain the solid orange (light gray) or dashed red curves, the optical potential has locally been shifted rigidly outward or inward by $dz = 1.0a_0$, respectively. In this way, the spatial region where the optical potential acts has been extended or shortened by $1.0a_0$. The spectra have been calculated for a photon energy $\hbar\omega_p = 21.2$ eV and *p*-polarized light incident under an angle of $\theta = 15^\circ$.

The optical potential is set constant throughout the slab and decays proportional to the electronic density into the vacuum region. The slight influence of a different choice of the extent of the optical potential into the vacuum region on the peak intensities has been tested and the result is shown in Fig. 7.

As the optical potential is assumed to be energy-independent in the present simulations, a typical electron energy has to be chosen such that the imaginary part of the optical potential is set equal to the imaginary part of the self-energy⁹⁰ at that particular energy. To this purpose we have chosen the energy of an electron excited by one photon from about 1 eV below the valence-band maximum.

In the present simulations the real part of the optical potential has been set equal to zero. We note, however, that a band-gap correction, as is commonly introduced by a scissor operator, can easily be included by adding a spatially constant real part to $v_{\text{opt}}(z)$. In case of 1PPE this shift has not been considered explicitly, because within the golden rule formulation for the 1PPE photocurrent it is equivalent to a shift of the photon energy.

F. Symmetry of Si(001) $p(2 \times 2)$ and dipole selection rules for 1PPE in normal emission

Symmetry selection rules are a helpful tool to interpret the photoemission spectra taken with polarized light. Furthermore, the computational workload can be reduced by restricting the time propagation to those initial states that actually couple to the outgoing photoelectron states. Selection rules are particularly meaningful in case of normal emission because of the high symmetry of the outgoing electron wave function.

Due to the surface-induced modification of the electronic structure and the small escape depth of the elastically scattered

TABLE I. Characters of the (irreducible representations of the) symmetry group C_{2v} .

C_{2v}		E	C_2	σ_v	σ'_v
A_1	z	1	1	1	1
A_2	xy	1	1	-1	-1
B_1	x	1	-1	1	-1
B_2	y	1	-1	-1	1

photoelectrons, the selection rules are governed by the 2D symmetry group of the surface rather than the 3D space group relevant for, for example, optical transitions in the bulk. Dipole selection rules for optical transitions in the fcc and bcc lattices are, for instance, tabulated in the paper by Eberhardt and Himpfel.¹¹¹

The 2D space-group of the $p(2 \times 2)$ reconstruction of Si(001) is pmg . Due to the glide plane it is not symmorphic. At $\bar{\Gamma}$ the 2D point group of the wave vector is C_{2v} . There are four 1D irreducible representations of the C_{2v} (Ref. 112) (see Table I).

If the electric field vector points along one of the coordinate axes, the dipole operator transforms according to the irreducible representations B_1 (for the x direction), B_2 (for the y direction), and A_1 (for the z direction).

In case of 1PPE the photocurrents could be calculated from Fermi's golden rule formula (1). We assume the dipole approximation for \mathbf{A} . In case of normal emission, the final state $|f\rangle$ describing the outgoing photoelectron is A_1 symmetric. Hence, there are nonvanishing matrix elements only if the initial state $|i\rangle$ transforms according to the same irreducible representation as the dipole operator. Thus, as long as one remains within the linear regime, the computational workload can be reduced by omitting initial states that do not couple. We have carried through test calculations that confirm that the spectra are not affected by this procedure. States that do not couple have thus been omitted from the simulations presented below.

Furthermore, for an arbitrary orientation of the polarization, described by the vector \mathbf{A} , we observe that the mixed terms in the matrix element vanish due to the fact that for an initial state with a given symmetry only one of the matrix elements with respect to \hat{p}_x , \hat{p}_y , and \hat{p}_z can be nonzero:

$$|\mathbf{A} \cdot \langle i | \hat{\mathbf{p}} | f \rangle|^2 = |A_x|^2 |\langle i | \hat{p}_x | f \rangle|^2 + |A_y|^2 |\langle i | \hat{p}_y | f \rangle|^2 + |A_z|^2 |\langle i | \hat{p}_z | f \rangle|^2. \quad (52)$$

Thus, within the approximation of one single active electron, 1PPE spectra for arbitrary polarization can be calculated from the three spectra with the electric field pointing into one of the coordinate directions. This has been exploited to create the spectra in Figs. 8 and 9. We emphasize that the simplifications described above only hold in case of 1PPE. In case of multiphoton photoemission, an individual simulation is required for each direction of the electric field vector of the light wave. Furthermore, the selection rules for the initial states are less restrictive and hence more states have to be propagated within the simulation. Thus, the present code can be used to calculate, for instance, 2PPE spectra, but the computational effort will be somewhat larger.

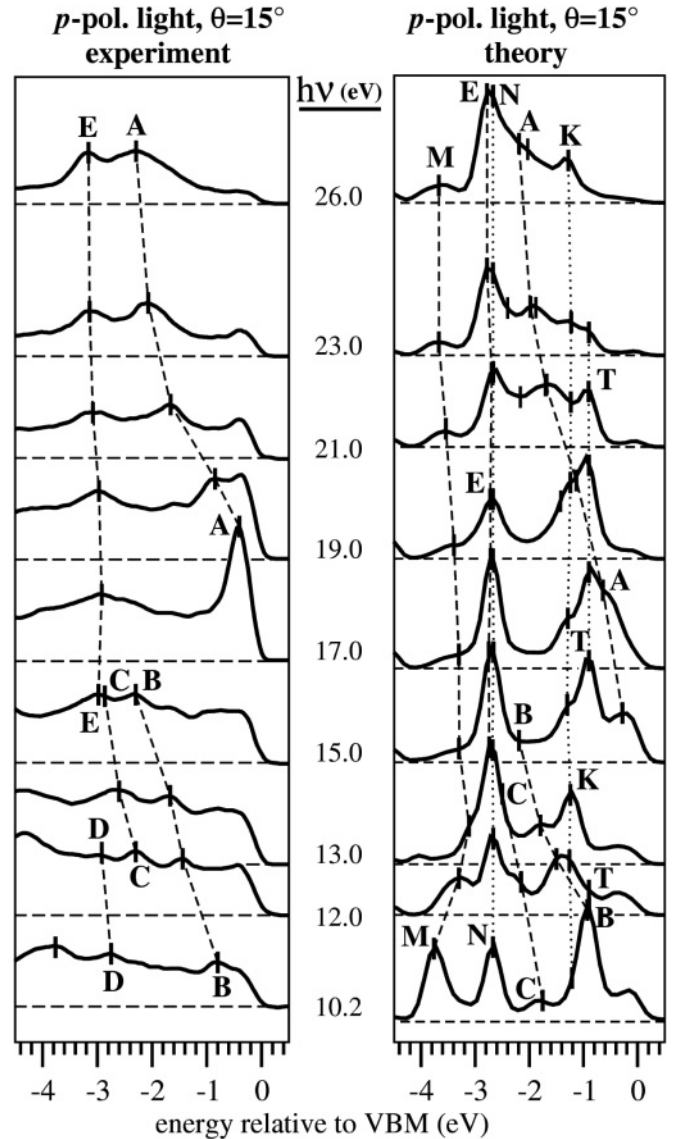


FIG. 8. Experimental (left) and calculated (right) normal emission photoemission spectra for the Si(001) surface for p -polarized light incident under an angle of $\theta = 15^\circ$ with respect to the surface normal. $h\nu$ denotes the photon energy. The theoretical photocurrents have been averaged with respect to the (1×2) and (2×1) domains of the Si(001) surface reconstruction, with the plane of incidence being either parallel or perpendicular to the direction of the dimer rows. The experimental spectra have been extracted (digitized) from Fig. 4 of the work by Johansson *et al.* (Ref. 96). The peak positions and denominations have been adopted from the original work by Johansson *et al.* Moreover, motivated by our theoretical results, an additional peak has been marked without label in the experimental spectra. Its position has been derived by visual inspection and thus should only be considered as a rough estimate of the true peak position.

G. Simulated Si(001) 1PPE spectra at normal emission

The theoretical spectra for several photon energies in the range $\hbar\omega_p = 10$ –26 eV and an angle of incidence of the light $\theta = 15^\circ$ and $\theta = 45^\circ$ are displayed in Figs. 8 and 9, respectively (for the values of the optical potential, see Table II). They are compared to experimental Si(001)

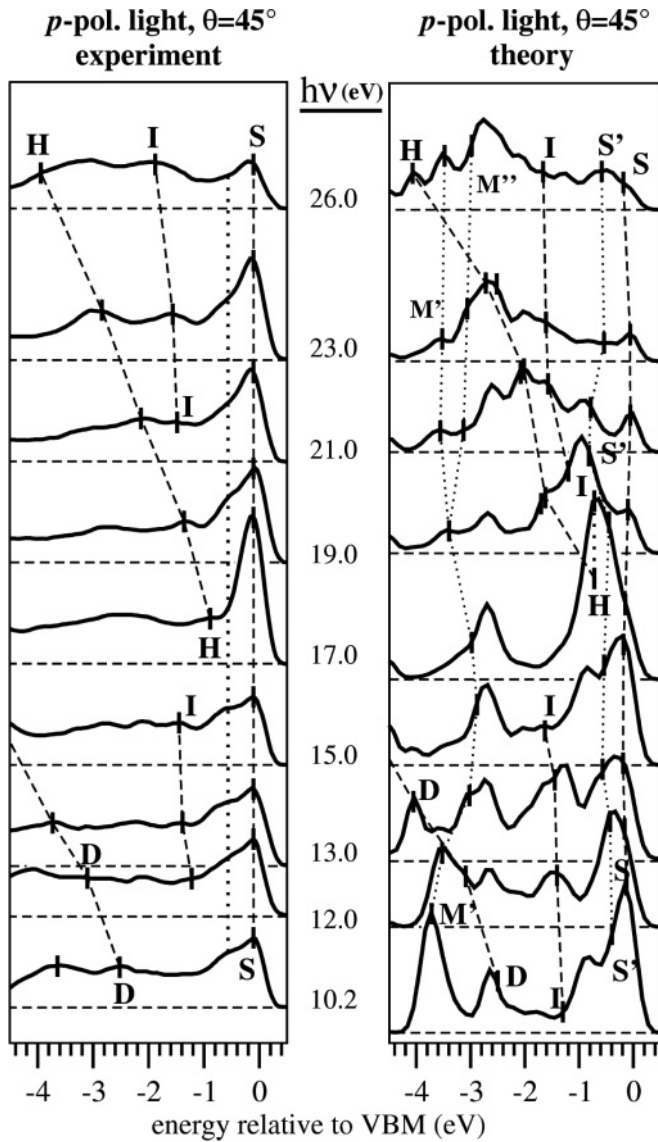


FIG. 9. Same as Fig. 8 but for an incidence angle of $\theta = 45^\circ$. Only peaks that are present by virtue of the field component perpendicular to the surface have been marked in the theoretical spectra. The experimental spectra have been extracted (digitized) from Fig. 5 of the work by Johansson *et al.* (Ref. 96). Peak positions and denominations have been adopted from their original work. To aid the comparison to the theoretical results, additional peaks derived from visual inspection have been marked without label in the experimental spectra. The peak *S* attributed to the surface dimers has a shoulder at higher binding energies, which is marked qualitatively by the dotted line. It is attributed to a second Si-dimer-derived peak.

photoemission spectra by L. S. O. Johansson *et al.*, which have been extracted from Figs. 4 and 5 of Ref. 96.

The peaks in the experimental spectra are labeled according to the original denominations of Johansson *et al.* The corresponding peaks in the theoretical spectra are denoted by the same letters. A first comparison shows that almost all structures identified in experiment find a correspondence in the theoretical spectra. Additional features in the computed spectra can be identified on the basis of the calculations. The initial states resulting in these peaks are discussed below.

TABLE II. Values of the imaginary part of the optical potential used in the simulations as a function of photon energy $\hbar\omega_p$. They were estimated by reading off typical values for the imaginary part of the self-energy from Fig. 3 in Ref. 90 by Fleszar and Hanke. In the present photoemission calculations, the real part of the optical potential has been set equal to zero.

Photon energy $\hbar\omega_p$ (eV)	Optical potential $\text{Im}V_{\text{opt}}$ (eV)
10.2	0.40
12.0	0.60
13.0	0.70
15.0	0.85
16.85	1.00
19.0	1.20
21.2	1.45
23.0	1.62
26.0	1.85

When comparing to experiment one has to consider that the background of inelastically scattered electrons is absent in the theoretical spectra.

The origin of the peaks in the calculated photoemission spectra can be revealed by decomposing the spectra into contributions from different initial state bands or into contributions arising from specific polarization of the light (i.e., with the electric field vector pointing parallel to one of the Cartesian axes). Figures 10 and 11 illustrate these considerations. Figure 10 corresponds to an electric field vector in the surface plane. It is the sum of the two spectra for the electric field oriented in x and y directions, respectively. Figure 11 has been calculated for an electric field vector of the light perpendicular to the surface (i.e., pointing into the z direction). The final theoretical spectra in Figs. 8 and 9 are superpositions of these spectra weighted with the appropriate geometry factors. As pointed out above, only initial states of definite symmetry contribute to the spectra with the electric field parallel to one of the coordinate axes. This allows for an identification of the origin of the peaks at arbitrary angles. The capital letters in the figures classify the contributions to the photocurrent according to the initial state from which they originate.

The primary information contained in photoemission spectra are the positions of the maxima, from which the binding energy of the respective states are deduced. Due to the \mathbf{k}_\perp dispersion, photoemission peaks derived from bulk states disperse with photon energy. In Figs. 12 and 13 and in Figs. 15 and 16 we compare the peak positions in the experimental and theoretical spectra as a function of photon energy.

The initial-state Kohn-Sham bulk bands relevant for normal emission are shown in Figs. 14 and 17, together with surface resonances that have been identified in the theoretical spectra. The wave vectors in Fig. 17 are folded back onto the Δ line if the scattering by the $p(2 \times 2)$ surface reconstruction is taken into account. Moreover, the assignment of the photoemission peaks to the respective initial states is marked by the labels at the vertical arrows.

For the analysis of the initial-state contributions to the photoemission spectra, bulk states have been assigned to the

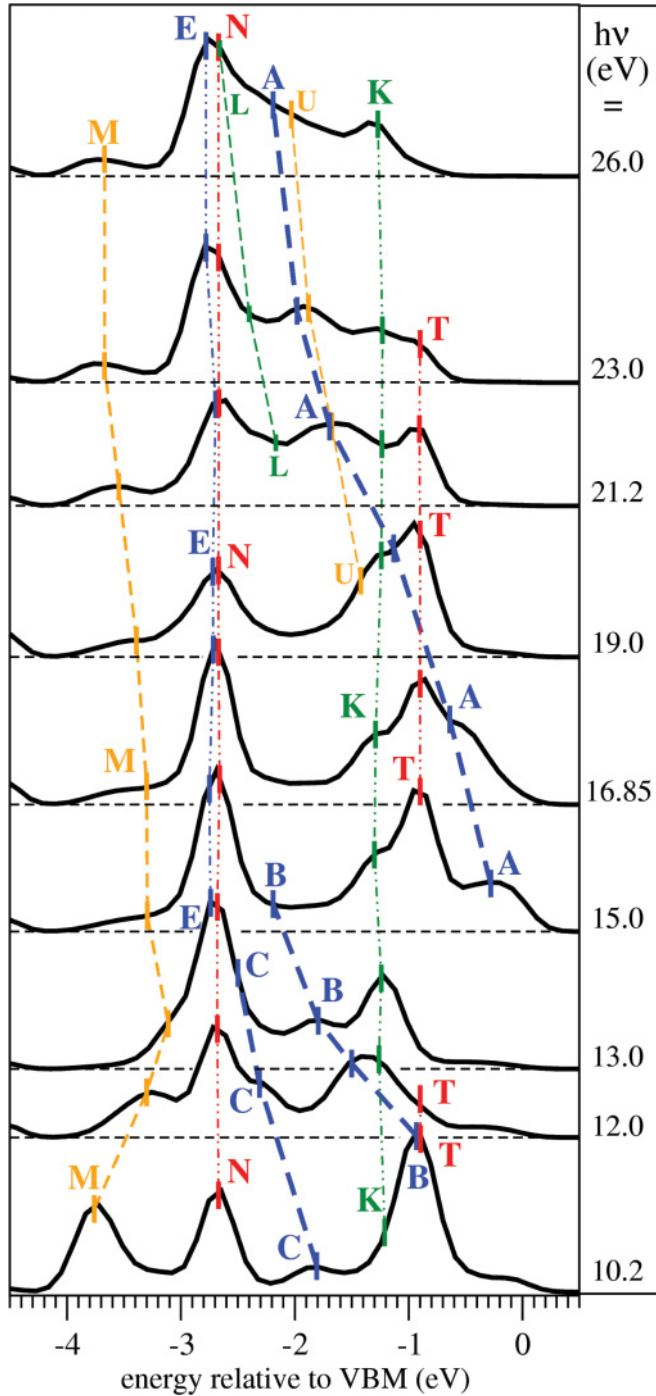


FIG. 10. (Color online) Polarization analysis for the Si(001) $p(2 \times 2)$ normal-emission spectra. Here the spectra have been calculated for angle of incidence of the light $\theta = 0^\circ$; that is, the electric field vector lies in the surface plane and is either parallel or perpendicular to the direction of the dimer rows. The spectra have been averaged with respect to these two orientations, corresponding to an average over the (2×1) and (1×2) dimerized terraces on the Si(001) surface. As a guide to the eye, peaks have been connected by dashed or dotted lines.

initial states from the slab calculation in the following way: The plane-wave expansion of the Kohn-Sham states from the slab calculation is subdivided into four contributions, each containing all wave vectors of the form $\mathbf{G} + \nu_1\pi/a\mathbf{e}_x + \nu_2\pi/a\mathbf{e}_y$,

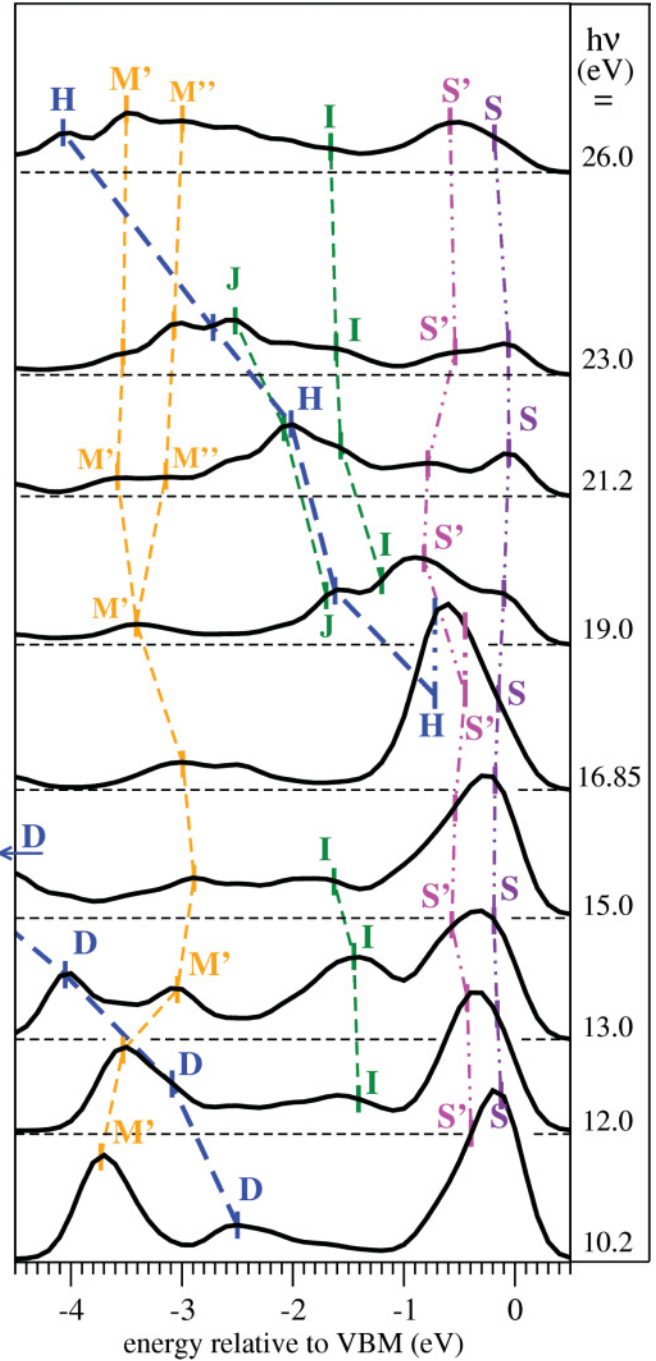


FIG. 11. (Color online) Same as Fig. 10 but for grazing incidence ($\theta = 90^\circ$) and electric field vector of the light perpendicular to the Si(001) surface. As compared to the spectra in Fig. 10 an additional scaling factor of 1/2 has been applied. In addition, the spectra in this figure have been convoluted with a Gaussian of width 100 meV.

$\nu_1, \nu_2 \in \{0, 1\}$. \mathbf{G} denotes the reciprocal lattice vectors of the supercell with (1×1) surface unit cell. a is the surface lattice constant of Si(001) (1×1) . If one of the wave vectors $\nu_1\pi/a\mathbf{e}_x + \nu_2\pi/a\mathbf{e}_y$ dominates, the orbital from the slab calculation is assigned to the respective rod in reciprocal space. If there is more than one relevant admixture, it is assigned to all of the respective bulk states. We expect this to be the case for surface states or bulk states with strong surface scattering.

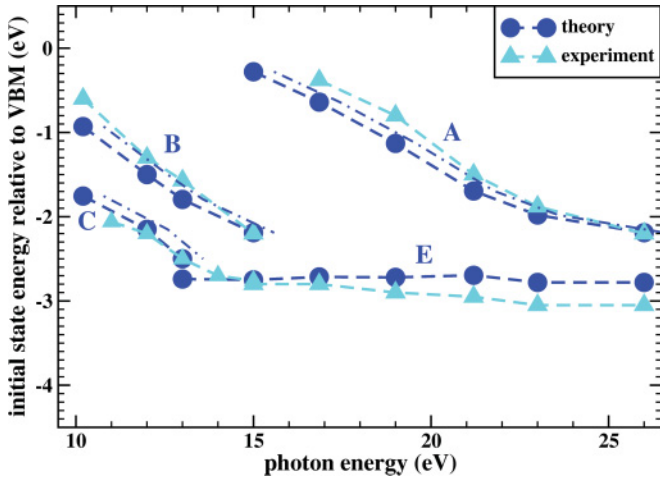


FIG. 12. (Color online) Dispersion of the peaks *A*, *B*, *C*, and *E* observed in the calculated and experimental spectra for angle of incidence of the light $\theta = 15^\circ$ (see Figs. 8 and 10). These peaks arise from initial states which can be ascribed to the Δ_5 -bulk band and require no backfolding (see Fig. 14). The circles and triangles represent the theoretical and experimental peak positions, respectively. To account for the difference between quasiparticle energies and the Kohn-Sham eigenenergies, the dash-dotted lines have been obtained from the calculated peak positions by a rigid shift of 0.58 eV [the band-gap correction (Ref. 90)] toward higher photon energies. See Sec. III E.

Emission from bulk bands that require no backfolding is characteristic for the peaks labeled *A*, *B*, *C*, *D*, *E*, and *H*. In the online version of this paper the respective contributions are marked in blue in Figs. 10–17. The structures denoted *I*, *J*, *K*, and *L* require a 2×1 backfolding [i.e., they should be present also for a (2×1) reconstructed surface]. They are marked in green. *M*, *M'*, *M''*, and *U* require a further backfolding also perpendicular to the dimer bonds; these contributions

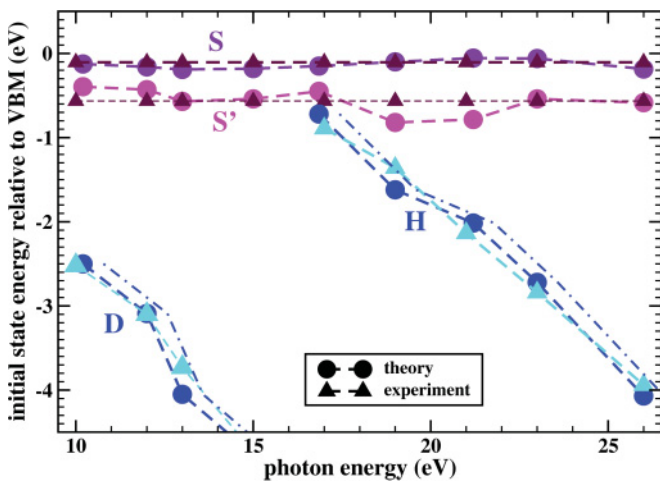


FIG. 13. (Color online) Same as Fig. 12, but for angle of incidence of the *p*-polarized light $\theta = 45^\circ$ and the peaks *D*, *H*, *S*, and *S'* (see the spectra in Figs. 9 and 11) that are due to emission from the Δ_2 -bulk band (without backfolding) and to the dangling-bond states D_{up} and D'_{up} (cf. Fig. 14). Labels and colors correspond to Fig. 11. Rough estimates for the peak positions *S'*, and in parts also for *D*, have been derived from inspection of the experimental spectra.

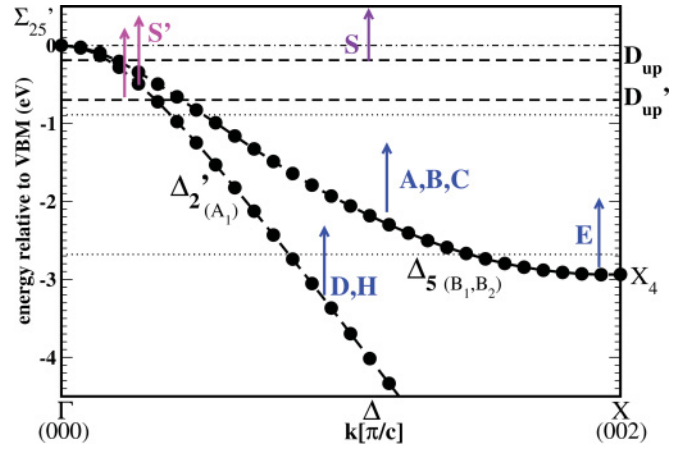


FIG. 14. (Color online) Initial states of photoemission. Bulk band structure of the Kohn-Sham eigenenergies of Si along the Δ line. In addition to the Δ_5 - and Δ_2 -bulk bands the energies of the D_{up} - and D'_{up} -surface resonances are marked by horizontal lines. Transitions identified above are indicated by arrows. Labels and colors correspond to Figs. 10 and 11.

are marked in orange. Finally, *S*, *S'*, *T*, and *N* are features associated with surface resonances, which are marked in violet, magenta, or red.

In the rest of this section we give details of the origin of the individual peaks observed in the calculated spectra and compare to the experimental peaks and assignments of Johansson *et al.* (cf. Fig. 1 in Ref. 96). The polarization is abbreviated by \perp and \parallel if the electric field vector of the incident light wave is perpendicular to the surface or lies within the surface plane. First we consider the *nondispersing features* *S* at about -0.15 eV relative to the valence-band maximum (VBM) and *S'*, which lies in the range between -0.4 and -0.8 eV, furthermore the structures denoted by *T* and *K* at -0.9 eV and -1.2 to -1.3 eV, respectively, as well as the prominent peak labeled *N* or *E* at about -2.7 eV.

(1) The peaks *S* and *S'* appear over the whole range of photon energies. They can be ascribed to emission from the *dangling-bond resonances* D_{up} and D'_{up} , respectively. Note that there are two occupied dangling-bond resonances at $\bar{\Gamma}$ due to the $p(2 \times 2)$ reconstruction. In our slab calculation, the D_{up} -state at $\bar{\Gamma}$ lies between -0.10 and -0.20 eV, close to the value of -0.10 to -0.15 eV determined experimentally and theoretically.^{12,13,15} D'_{up} forms a broad resonance with the Δ_2 -bulk band with center at around -0.7 eV at $\bar{\Gamma}$ (cf. Ref. 15). This resonance width permits the observed shifts in the position of peak *S'* with varying photon energy.

In Ref. 96 Johansson *et al.* point out that there is a low-energy shoulder of the surface-derived peak *S*, which is not marked explicitly in the original spectra. For clarity, we have indicated an approximate position of this shoulder in the experimental spectra in Fig. 9 by a dotted line and adopted this in Fig. 13. For the presence of the D'_{up} state in photoemission from the Si(001) surface we refer the reader to the papers by Landmark *et al.*,¹¹³ Enta *et al.*,¹¹⁴ and Johansson *et al.*¹¹⁵ At lower photon energies the relative emission intensities from the dangling-bond states—as compared to the rest of the spectrum—seem to agree with experiment. However, for

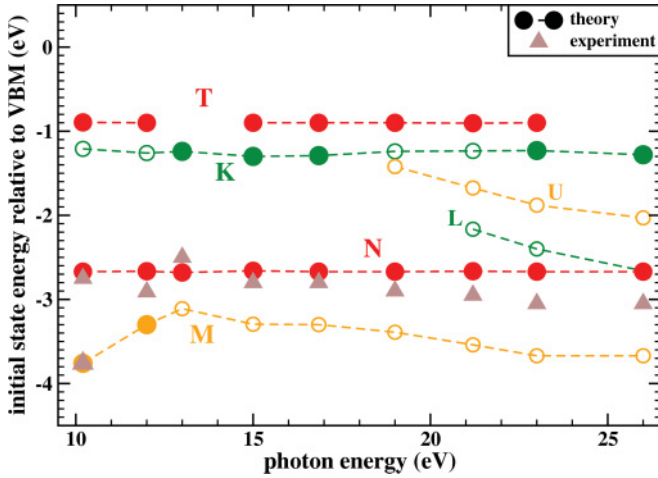


FIG. 15. (Color online) Dispersion of additional peaks M , N , T , U , K , and L not contained in Fig. 12 observed in the calculated photoemission spectra for angle of incidence of the light $\theta = 15^\circ$. As these peaks have been derived from local maxima in symmetry-specific partial contributions to the photoemission spectrum, not all of them can easily be identified in the total spectrum. See text for details. Weak features are marked by open circles. The peaks in this viewgraph originate either from backfolded bulk bands at $\bar{\Gamma}$ (K , L , M , and U denoted by green and orange circles) or the two surface resonances (T and N denoted by red circles). See Fig. 17 for the initial states. For comparison, selected peak positions from the experimental spectra in Fig. 8 are denoted by triangles. This includes the peak with the highest binding energy in the $h\nu = 10.2$ eV spectrum, as well as peaks D , C , and E in the spectra taken at increasingly larger photon energy. When comparing to experiment, one should keep in mind that peak M is comparatively weak in the theoretical spectra, save for the lowest photon energies. For a detailed comparison, see text.

photon energies between 19 and 23 eV, the relative intensity in the dangling-bond state peak S is considerably higher in the experimental than in the calculated spectra.

(2) There is another nondispersing peak in the upper part of the spectrum at around -0.89 eV labeled T . This structure is excited by the electric field component parallel to the dimer bonds only and thus due to emission from an initial state of B_1 symmetry, most likely forming part of a *dangling-bond resonance*. Emission from this state is strong at photon energies $\hbar\omega_p = 10.2$ eV and $\hbar\omega_p = 15$ – 21 eV, but it is nearly missing for $\hbar\omega_p = 13$ and 26 eV. At $\hbar\omega_p = 10.2$ eV peak T is crossed by the dispersing structure B that is comparably weak at the other photon energies, and between $\hbar\omega_p = 17$ eV and $\hbar\omega_p = 19$ eV peak A disperses through the region. Thus, T appears mainly as an enhancement in the emission from the bulk band Δ_5 that is underlying the dispersing structures A and B (see below). Possibly, this feature may also occur in the experimental spectra, although for any instance weaker and not marked explicitly.

(3) Present in the theoretical spectra more or less throughout the whole range of photon energies there is a peak labeled K at about -1.3 eV. This peak can be traced back to emission from a *nearly flat bulk band* along the Σ - L line (see Fig. 17, cf. Kentsch *et al.*,¹² where L'_3 is determined at -1.27 eV). We attribute K to the high density of states of this band (DOS-peak). Since this band is of B_2 symmetry, which means that it

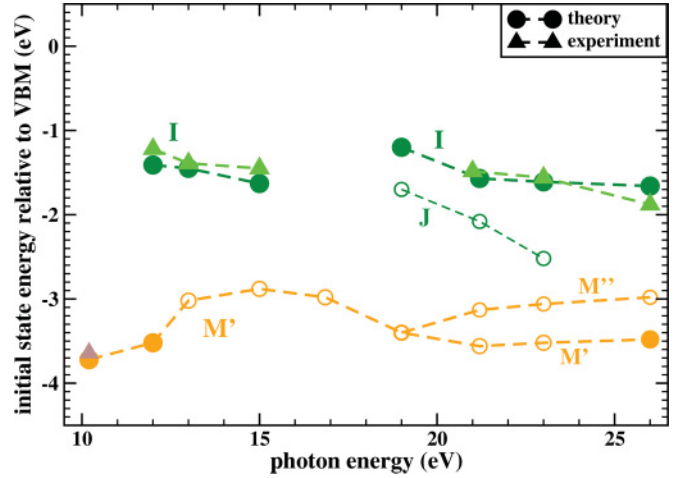


FIG. 16. (Color online) Same as Fig. 15, but for angle of incidence of the p -polarized light $\theta = 45^\circ$ and the peaks M' , M'' , I , and J (see spectra in Figs. 9 and 11). The peaks in this viewgraph originate from backfolded bulk bands at $\bar{\Gamma}$. See Fig. 17 for the initial states. For comparison, selected peak positions from the experimental spectra in Fig. 9 are denoted by triangles. For a detailed comparison to experiment, see text.

has negative mirror parity (as is indicated by the minus sign in Fig. 17), normal emission from this band is excited by the electric field component in the surface plane perpendicular to the dimer bonds. We have not been able to attribute peak K to a feature observed in the experimental spectra.

(4) The pronounced peak at about -2.7 eV in the theoretical spectra consists of two different components. One contribution that we have denoted by N stems from a *back bond-related surface resonance* of B_2 -symmetry that is located at -2.68 eV in our slab calculation. The resonance is formed with the Δ_5 -bulk band of B_2 symmetry. Consequently, this contribution is excited by the field component parallel to the dimer rows. In the experimental spectrum for $\hbar\omega_p = 10.2$ eV, the peak D that

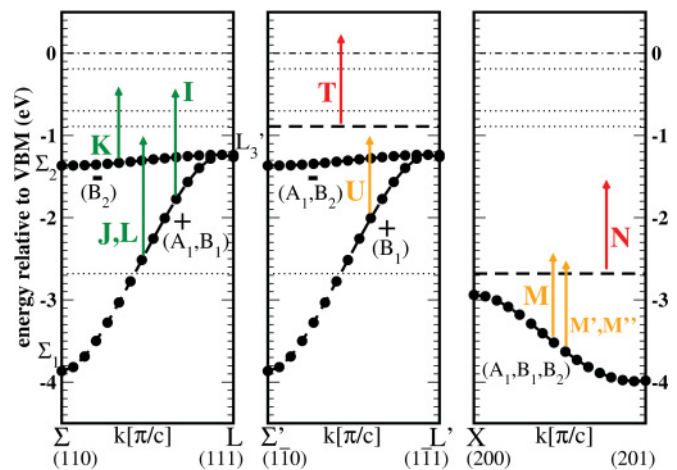


FIG. 17. (Color online) Initial states of photoemission (continued). Bulk band structure of the Kohn-Sham eigenenergies of Si along three lines in reciprocal space, which are folded back to the Δ line in case of the $p(2 \times 2)$ reconstruction. In addition, the positions of two (presumably dangling-bond- and back bond-related) surface resonances are noted. Transitions are marked similar as in Fig. 14.

was not ascribed to a bulk band transition by Johansson *et al.*, seems to coincide with our peak N .

We have identified a second component denoted by E at an energy of -2.85 to -2.88 eV which we interpret as a DOS peak owing to the high density of states close to the bottom of the doubly degenerate Δ_5 -bulk band. Actually, the bottom of this band at the X point lies a little lower at about -2.95 to -3.0 eV (Kentsch *et al.*¹² have found a value of -2.97 eV). The peak is discernible for photon energies above 13 eV and becomes stronger with increasing photon energy. This peak can be identified with the corresponding peak E in the experimental spectra. However, there is a shift of 100–300 meV to higher binding energies in the experimental data that becomes most pronounced for the highest photon energies.

Now we turn to the *dispersing features*. These are the peaks denoted by A , B , and C in the spectra for \parallel polarization and by D and H in the spectra for \perp polarization as well as the peaks M and M' , M'' . Furthermore, there is a group of dispersing peaks labeled L and U in the spectra for \parallel polarization and by I and J in the spectra for \perp polarization that are discernible only for a range of photon energies of some eV.

(5) The peaks A and B within the upper and lower range of photon energies have their origin in the Δ_5 -bulk band (cf. the ascription of Johansson *et al.*). In fact, the Δ_5 band is doubly degenerate (with contributions from atomic Si p_x and p_y orbitals). The states have B_1 and B_2 symmetry with respect to C_{2v} . These bands yield contributions to the photocurrent of comparable intensity for the appropriate electric field components in the surface plane. Also originating from the Δ_5 -bulk bands, but from k points closer to the X point, the peak C disperses from about 1.75 eV downward to finally merge into peak E —in both theory and experiment—at a photon energy of about 15 eV. The dispersion of all three structures is in agreement with the experimental findings, in particular if the shift of photon energy—correcting for the LDA band gap—is taken into account (see Fig. 12).

(6) Similarly, the peaks D and H arise from the Δ'_2 -bulk band, which disperses more steeply along the Δ line than the Δ_5 band. The peak H in the upper range of photon energies has also been identified in the experimental spectra, and the dispersion agrees well (cf. Fig. 13). For the theoretical structure D , there are corresponding peaks in the experimental spectra, which have been marked for photon energies from $\hbar\omega_p = 8$ eV to $\hbar\omega_p = 12$ eV in the original spectra. To compare to theory, we have attempted to extrapolate this structure to higher photon energies in Fig. 9. At about 17 eV, there is a strongly enhanced emission where H crosses the energy range of the surface resonance peaks S and S' . This is observed both in theory and in experiment.

(7) Peak M as well as peaks M' and M'' , which branches off from M' at a photon energy of 19 eV, can be ascribed to emission from the bulk band displayed in the right panel of Fig. 17, which is dispersing from 2.9 eV down to 4.0 eV. This band is threefold degenerate; the states have A_1 , B_1 , and B_2 symmetry with respect to C_{2v} . It contributes to the photocurrent for all polarizations of the incident light. Although the respective peaks can be tracked through all photon energies in the calculated spectra, the emission is strong only for the lowest photon energies, in particular for

$\hbar\omega_p = 10.2$ eV. At this energy there is a peak at about the same binding energy in the experimental spectra (not explicitly marked in Ref. 96). Its approximate position has been added to Figs. 8 and 15 as well Figs. 9 and 16.

(8) The peaks denoted by L in the \parallel -polarization spectra and by I and J in the \perp -polarization spectra originate from the dispersing bulk band signified by “+” in the left panel of Fig. 17. The states have two symmetries, A_1 and B_1 , with respect to C_{2v} . The states of B_1 symmetry yield peak L , while the states of A_1 symmetry yield peaks I and J . The occurrence of peak I at lower and higher photon energies has also been identified in the experimental spectra for $\theta = 45^\circ$ with roughly the same small dispersion (see Fig. 16). As for the features labeled L and J in the theoretical spectra one has to bear in mind that they were elicited from one of the contributions to the photocurrent after the complete (also with respect to backfolding) decomposition of the theoretical spectra. These features cannot be clearly detected from an inspection of the spectra alone, since peak J is nearly degenerate with H , and L partially fills the energy range between peaks N and A .

(9) The preceding point also holds for the peak labeled U in the theoretical spectra at higher photon energies in case of \parallel polarization. It is overlapping with A , and for this reason it cannot be clearly distinguished from A only by inspection of the spectrum itself. Close inspection of the wave functions suggests that there is a feature U that goes back to the dispersing bulk band of B_1 symmetry displayed in the middle panel in Fig. 17 (bulk bands backfolded in dimer row direction).

Altogether, the assignment of the peaks to the valence bands and surface states as well as the peak dispersion are generally in good agreement with the experimental data.⁹⁶ The relative intensity of the emission from the dangling-bond peaks is not reproduced well at all photon energies. We speculate that this may be due to dynamical screening of the laser field at the surface, which is neglected in the frozen effective-potential approach (see, e.g., Refs. 116–120). Although certainly an important aspect, the refraction of the light has not been considered in this work. Application of the Fresnel equations to the optical refraction problem implies an unphysical jump of the component of the electric field perpendicular to the surface. If the nonlocal screening response is considered in the surface region the resulting electric field becomes continuous.¹²¹ We note that the screening of the normal component of the electric field can, in principle, be calculated within a self-consistent TDDFT simulation as long as retardation effects can be neglected. This will be the direction of future work.

Beside this source of possible deviations of the intensities from experiment, it should also be kept in mind that the inelastic scattering events are represented only in a very approximate way by the optical potential operator.

Furthermore, we observe that there are apparently additional or considerably stronger photoemission peaks in theory than in experiment, which are derived from valence states backfolded by the 2×2 reconstruction (e.g., peaks M , N , T at certain photon energies). Additional calculations for a 2×1 reconstructed Si(001) surface with buckled dimers indeed confirm that these features vanish in the 2×1 normal emission spectra. The photoemission experiments⁹⁶ were performed at

room temperature, that is, above the order-disorder transition of the dimer buckling orientation.^{122,123} Nonetheless, a strong local $2 \times$ antibuckling correlation is known to persist up to room temperature, which is reflected by the observation of $2 \times$ backfolded states in room-temperature photoemission spectra.^{113,114,124} The smaller intensity of the backfolded bands in the experimental room-temperature photoemission spectra as compared to the calculated spectra may be ascribed to the temperature-induced disorder of the $2 \times$ dimer antibuckling surface reconstruction.^{113,114} We note that the lowest energy structure from DFT is the $c(4 \times 2)$ reconstruction.¹⁰¹ However, the energy difference to the $p(2 \times 2)$ reconstruction is known to be of the order of a few meV per dimer,¹⁰¹ switching is possible even by an applied electrical field.¹²⁵ As the photoemission experiments were performed at room temperature, correlations between neighboring dimer rows are expected to be very much smaller than “antibuckling correlations” within a single row. Thus, any structure in the theoretical normal emission spectra associated with the relative phases of the dimer buckling in neighboring dimer rows should be “washed out” in the experimental room-temperature spectra.

IV. SUMMARY AND OUTLOOK

A method for the *ab initio* calculation of photoemission spectra excited by fs-laser pulses has been developed. The emission process is simulated in the time domain, and the angle- and energy-resolved spectra are calculated from the Fourier transform of the time-dependent single-particle wave functions. An optical potential, estimated from theoretical data for the energy-dependent self-energy of bulk Si by Fleszar and Hanke,⁹⁰ is taken to approximately account for the finite mean free path of the photoelectrons due to inelastic electron-electron scattering. In that case, the effective potential from the ground-state DFT calculation has to be assumed frozen during the whole simulation.

Normal-emission photoemission spectra for the Si(001) surface have been calculated and compared to experiment to demonstrate our approach. The detailed analysis of the spectra results in an assignment of photoemission peaks to valence bands and surface states. We obtain an overall good agreement with the peak dispersion observed experimentally. Deviation of the photoemission peak intensities may partially be due to approximations in the theory, for example, the neglect of screening of the laser field, the neglect of thermal disorder, and the very rough description of inelastic electron scattering by the optical potential.

The direct simulation is not intended as a substitute for the Fermi’s golden rule type of approaches that have successfully been applied to describe 1PPE spectra.¹ As our simulation is nonperturbative, the time-dependent wave functions inherently contain also the higher-order contributions to the photocurrent. In particular, the 2PPE spectra can easily be derived from the same kind of simulations. Moreover, we expect that the direct simulation of the photoemission process in the time domain may facilitate future studies of multiphoton photoemission, pump-probe photoemission experiments with ultrashort laser pulses, and photoemission at high electronic excitation densities. The purpose of the present study is to present the technical framework and demonstrate the feasibility of the nonperturbative direct approach to photoemission. Improvements of the approximations applied, for example, the optical potential and the frozen effective potential, are certainly desirable.

ACKNOWLEDGMENTS

We are grateful to L. S. O. Johansson for permission to use his photoemission spectra from Ref. 96 and to M. Bonitz for pointing our attention to the Kramers-Henneberger transform. Financial support by the Innovationsfond des Landes Schleswig-Holstein is gratefully acknowledged. The numerical computations have been carried through at the Rechenzentrum der Universität Kiel.

*husser@theo-physik.uni-kiel.de

¹W. Schattke and M. A. van Hove (editors), *Solid-State Photoemission and Related Methods. Theory and Experiment* (Wiley-VCH, Berlin, 2003).

²S. Hüfner, *Photoelectron Spectroscopy. Principles and Applications* (Springer, Berlin, 2003).

³S. D. Kevan, *Angle-Resolved Photoemission: Theory and Current Applications* (Elsevier, Amsterdam, 1992).

⁴L. Kipp, K. Roßnagel, C. Solterbeck, T. Strasser, J. W. Schattke, and M. Skibowski, *Phys. Rev. Lett.* **83**, 5551 (1999).

⁵A. Damascelli, Z. Hussain, and Z.-X. Shen, *Rev. Mod. Phys.* **75**, 473 (2003).

⁶E. E. Krasovskii, K. Roßnagel, A. Fedorov, W. Schattke, and L. Kipp, *Phys. Rev. Lett.* **98**, 217604 (2007).

⁷F. J. Himpsel and T. Fauster, *J. Vac. Sci. Technol. A* **2**, 815 (1984).

⁸H. Ueba and B. Gumhalter, *Prog. Surf. Sci.* **82**, 193 (2007).

⁹H. Petek and S. Ogawa, *Prog. Surf. Sci.* **56**, 239 (1997).

¹⁰M. Weinelt, *J. Phys. Condens. Matter* **14**, R1099 (2002).

¹¹K. I. Shudo and T. Munakata, *Phys. Rev. B* **63**, 125324 (2001).

¹²C. Kentsch, M. Kutschera, M. Weinelt, T. Fauster, and M. Rohlfing, *Phys. Rev. B* **65**, 035323 (2001).

¹³M. Weinelt, M. Kutschera, T. Fauster, and M. Rohlfing, *Phys. Rev. Lett.* **92**, 126801 (2004).

¹⁴M. Weinelt, M. Kutschera, R. Schmidt, C. Orth, T. Fauster, and M. Rohlfing, *Appl. Phys. A* **80**, 995 (2005).

¹⁵M. Kutschera, M. Weinelt, M. Rohlfing, and T. Fauster, *Appl. Phys. A* **88**, 519 (2007).

¹⁶T. Brabec and F. Krausz, *Rev. Mod. Phys.* **72**, 545 (2000).

¹⁷D. B. Milošević, G. G. Paulus, D. Bauer, and W. Becker, *J. Phys. B* **39**, R203 (2006).

¹⁸P. B. Corkum and F. Krausz, *Nat. Phys.* **3**, 381 (2007).

¹⁹F. Krausz and M. Ivanov, *Rev. Mod. Phys.* **81**, 163 (2009).

²⁰J. Itatani, J. Levesque, D. Zeidler, H. Niikura, H. Pépin, J. C. Kieffer, P. B. Corkum, and D. M. Villeneuve, *Nature (London)* **432**, 867 (2004).

²¹P. J. Feibelman and D. E. Eastman, *Phys. Rev. B* **10**, 4932 (1974).

- ²²J. B. Pendry, *Surf. Sci.* **57**, 679 (1976).
- ²³G. D. Mahan, *Phys. Rev. B* **2**, 4334 (1970).
- ²⁴W. Schattke, E. E. Krasovskii, R. Díez Muiño, and P. M. Echenique, *Phys. Rev. B* **78**, 155314 (2008).
- ²⁵J. van Heys, M. Lindenblatt, and E. Pehlke, *Phase Transitions* **78**, 773 (2005).
- ²⁶K. C. Kulander, *Phys. Rev. A* **35**, 445 (1987).
- ²⁷J. Parker, K. T. Taylor, C. W. Clark, and S. Blodgett-Ford, *J. Phys. B* **29**, L33 (1996).
- ²⁸P. B. Corkum, *Phys. Rev. Lett.* **71**, 1994 (1993).
- ²⁹R. Grobe and J. H. Eberly, *Phys. Rev. Lett.* **68**, 2905 (1992).
- ³⁰D. Bauer, *Phys. Rev. A* **56**, 3028 (1997).
- ³¹D. Lappas and R. van Leeuwen, *J. Phys. B* **31**, L249 (1998).
- ³²M. Petersilka and E. K. U. Gross, *Laser Phys.* **9**, 1 (1999).
- ³³M. Lein, E. K. U. Gross, and V. Engel, *Phys. Rev. Lett.* **85**, 4707 (2000).
- ³⁴S. Bauch, K. Balzer, and M. Bonitz, *Eur. Phys. Lett.* **91**, 53001 (2010).
- ³⁵A. D. Bandrauk and H. Z. Lu, *Phys. Rev. A* **72**, 023408 (2005).
- ³⁶N. A. Nguyen and A. D. Bandrauk, *Phys. Rev. A* **73**, 032708 (2006).
- ³⁷K. C. Kulander, *Phys. Rev. A* **36**, 2726 (1987).
- ³⁸M. S. Pindzola, P. Gavras, and T. W. Gorczyca, *Phys. Rev. A* **51**, 3999 (1995).
- ³⁹N. E. Dahlen and R. van Leeuwen, *Phys. Rev. A* **64**, 023405 (2001).
- ⁴⁰J. Zanghellini, M. Kitzler, C. Fabian, T. Brabec, and A. Scrinzi, *Laser Phys.* **13**, 1064 (2003).
- ⁴¹D. Hochstuhl and M. Bonitz, *J. Chem. Phys.* **134**, 084106 (2010).
- ⁴²M. A. L. Marques, C. A. Ullrich, F. Nogueira, A. Rubio, K. Burke, and E. K. U. Gross (eds.), *Time-Dependent Density Functional Theory* (Springer, Berlin, 2006).
- ⁴³C. A. Ullrich, U. J. Gossmann, and E. K. U. Gross, *Ber. Bunsenges. Phys. Chem.* **99**, 488 (1995).
- ⁴⁴C. A. Ullrich and E. K. U. Gross, *Comments At. Mol. Phys.* **33**, 211 (1997).
- ⁴⁵C. A. Ullrich, *J. Mol. Struct.* **501-502**, 315 (2000).
- ⁴⁶D. Bauer and F. Ceccherini, *Opt. Express* **8**, 377 (2001).
- ⁴⁷X.-M. Tong and Shih-I Chu, *Phys. Rev. A* **57**, 452 (1998).
- ⁴⁸X.-M. Tong and Shih-I Chu, *Phys. Rev. A* **64**, 013417 (2001).
- ⁴⁹V. Vénier, R. Taïeb, and A. Maquet, *Laser Phys.* **13**, 465 (2003).
- ⁵⁰X. Chu and Shih-I Chu, *Phys. Rev. A* **70**, 061402(R) (2004).
- ⁵¹D. Dundas and J. M. Rost, *Phys. Rev. A* **71**, 013421 (2005).
- ⁵²E. P. Fowe and A. D. Bandrauk, *Phys. Rev. A* **81**, 023411 (2010).
- ⁵³R. Baer, D. Neuhauser, P. R. Ždánká, and N. Moiseyev, *Phys. Rev. A* **68**, 043406 (2003).
- ⁵⁴F. Calvayrac, P.-G. Reinhard, and E. Suraud, *Phys. Rev. B* **52**, R17056 (1995).
- ⁵⁵K. Yabana and G. F. Bertsch, *Phys. Rev. B* **54**, 4484 (1996).
- ⁵⁶C. A. Ullrich, P.-G. Reinhard, and E. Suraud, *J. Phys. B* **30**, 5043 (1997).
- ⁵⁷H. S. Nguyen, A. D. Bandrauk, and C. A. Ullrich, *Phys. Rev. A* **69**, 063415 (2004).
- ⁵⁸A. Pohl, P.-G. Reinhard, and E. Suraud, *Phys. Rev. Lett.* **84**, 5090 (2000).
- ⁵⁹A. Pohl, P.-G. Reinhard, and E. Suraud, *J. Phys. B* **34**, 4969 (2001).
- ⁶⁰A. Pohl, P.-G. Reinhard, and E. Suraud, *Phys. Rev. A* **68**, 053202 (2003).
- ⁶¹F. Calvayrac, P.-G. Reinhard, E. Suraud, and C. A. Ullrich, *Phys. Rep.* **337**, 493 (2000).
- ⁶²T. Fennel, K.-H. Meiwes-Broer, J. Tiggesbäumker, P.-G. Reinhard, P. M. Dinh, and E. Suraud, *Rev. Mod. Phys.* **82**, 1793 (2010).
- ⁶³L. P. Kadanoff and G. Baym, *Quantum Statistical Mechanics* (Benjamin, New York, 1962).
- ⁶⁴L. V. Keldysh, *Sov. Phys. JETP* **20**, 1018 (1965).
- ⁶⁵M. Bonitz (editor), *Progress in Nonequilibrium Green's Functions* (World Scientific, Singapore, 2000).
- ⁶⁶K. Balzer, S. Bauch, and M. Bonitz, *Phys. Rev. A* **81**, 022510 (2010).
- ⁶⁷G. Vignale, *Phys. Rev. B* **70**, R201102 (2004).
- ⁶⁸S. K. Ghosh and A. K. Dhara, *Phys. Rev. A* **38**, 1149 (1988).
- ⁶⁹E. Runge and E. K. U. Gross, *Phys. Rev. Lett.* **52**, 997 (1984).
- ⁷⁰M. van Faassen, P. L. de Boeij, R. van Leeuwen, J. A. Berger, and J. G. Snijders, *Phys. Rev. Lett.* **88**, 186401 (2002).
- ⁷¹N. T. Maitra, I. Souza, and K. Burke, *Phys. Rev. B* **68**, 045109 (2003).
- ⁷²F. Kootstra, P. L. de Boeij, and J. G. Snijders, *J. Chem. Phys.* **112**, 6517 (2000).
- ⁷³G. F. Bertsch, J.-I. Iwata, A. Rubio, and K. Yabana, *Phys. Rev. B* **62**, 7998 (2000).
- ⁷⁴C. Caroli, D. Lederer-Rozenblatt, B. Roulet, and D. Saint-James, *Phys. Rev. B* **8**, 4552 (1973).
- ⁷⁵P. L. de Boeij, *Lecture Notes in Physics*, Vol. 706 (Springer, Berlin, 2006), p. 287.
- ⁷⁶F. Kootstra, Ph.D. thesis, Rijksuniversiteit Groningen, 2001.
- ⁷⁷N. T. Maitra, K. Burke, and C. Woodward, *Phys. Rev. Lett.* **89**, 023002 (2002).
- ⁷⁸D. R. Hamann, M. Schlüter, and C. Chiang, *Phys. Rev. Lett.* **43**, 1494 (1979).
- ⁷⁹L. Kleinman and D. M. Bylander, *Phys. Rev. Lett.* **48**, 1425 (1982).
- ⁸⁰G. B. Bachelet, D. R. Hamann, and M. Schlüter, *Phys. Rev. B* **26**, 4199 (1982).
- ⁸¹D. R. Hamann, *Phys. Rev. B* **40**, 2980 (1989).
- ⁸²M. Fuchs and M. Scheffler, *Comput. Phys. Commun.* **119**, 67 (1999).
- ⁸³S. Ismail-Beigi, E. K. Chang, and S. G. Louie, *Phys. Rev. Lett.* **87**, 087402 (2001).
- ⁸⁴E. Luppi, H.-C. Weissker, S. Bottaro, F. Sottile, V. Vénier, L. Reining, and G. Onida, *Phys. Rev. B* **78**, 245124 (2008).
- ⁸⁵M. C. Payne, M. P. Teter, D. C. Allan, T. A. Arias, and J. D. Joannopoulos, *Rev. Mod. Phys.* **64**, 1045 (1992).
- ⁸⁶J. Neugebauer and M. Scheffler, *Surf. Sci.* **287/288**, 572 (1993).
- ⁸⁷J. E. Northrup, *Phys. Rev. B* **47**, 10032 (1993).
- ⁸⁸M. Rohlfing, P. Krüger, and J. Pollmann, *Phys. Rev. B* **48**, 17791 (1993).
- ⁸⁹M. Rohlfing, P. Krüger, and J. Pollmann, *Phys. Rev. B* **52**, 1905 (1995).
- ⁹⁰A. Fleszar and W. Hanke, *Phys. Rev. B* **56**, 10228 (1997).
- ⁹¹M. Førre, S. Selstø, J. P. Hansen, and L. B. Madsen, *Phys. Rev. Lett.* **95**, 043601 (2005).
- ⁹²C. Cohen-Tannoudji, J. Dupont-Roc, and G. Grynberg, *Introduction to Quantum Electrodynamics* (Wiley, New York, 1997).
- ⁹³R. Loudon, *The Quantum Theory of Light* (Clarendon Press, Oxford, 1983).
- ⁹⁴H. A. Kramers, *Collected Scientific Papers* (North-Holland, Amsterdam, 1956).
- ⁹⁵W. C. Henneberger, *Phys. Rev. Lett.* **21**, 838 (1968).

- ⁹⁶L. S. O. Johansson, P. E. S. Persson, U. O. Karlsson, and R. I. G. Uhrberg, *Phys. Rev. B* **42**, 8991 (1990).
- ⁹⁷T. Uda, H. Shigekawa, Y. Sugawara, S. Mizuno, H. Tochihara, Y. Yamashita, J. Yoshinobu, K. Nakatsuji, H. Kawai, and F. Komori, *Prog. Surf. Sci.* **76**, 147 (2004).
- ⁹⁸J. J. de Miguel, C. E. Aumann, R. Kariotis, and M. G. Lagally, *Phys. Rev. Lett.* **67**, 2830 (1991).
- ⁹⁹K. C. Low and C. K. Ong, *Phys. Rev. B* **50**, 5352 (1994).
- ¹⁰⁰P. Krüger and J. Pollmann, *Phys. Rev. Lett.* **74**, 1155 (1995).
- ¹⁰¹A. Ramstad, G. Brocks, and P. J. Kelly, *Phys. Rev. B* **51**, 14504 (1995).
- ¹⁰²W. Brenig and E. Pehlke, *Prog. Surf. Sci.* **83**, 263 (2008).
- ¹⁰³M. Bockstedte, A. Kley, J. Neugebauer, and M. Scheffler, *Comput. Phys. Commun.* **107**, 187 (1997).
- ¹⁰⁴R. S. Judson, D. J. Kouri, D. Neuhauser, and M. Baer, *Phys. Rev. A* **42**, 351 (1990).
- ¹⁰⁵G. L. Yudin, L. N. Gaier, M. Lein, P. L. Knight, P. B. Corkum, and M. Yu. Ivanov, *Laser Phys.* **14**, 51 (2004).
- ¹⁰⁶D. Neuhauser and M. Baer, *J. Chem. Phys.* **90**, 4351 (1989).
- ¹⁰⁷A. Vibok and G. G. Balint-Kurti, *J. Phys. Chem.* **96**, 8712 (1992).
- ¹⁰⁸D. Macías, S. Brouard, and J. G. Muga, *Chem. Phys. Lett.* **228**, 672 (1994).
- ¹⁰⁹L. Hedin, *Phys. Rev.* **139**, A796 (1965).
- ¹¹⁰F. Aryasetiawan and O. Gunnarsson, *Rep. Prog. Phys.* **61**, 237 (1998).
- ¹¹¹W. Eberhardt and F. J. Himpsel, *Phys. Rev. B* **21**, 5572 (1980).
- ¹¹²M. Wagner, *Gruppentheoretische Methoden in der Physik* (Vieweg, Stuttgart, 1998).
- ¹¹³E. Landemark, C. J. Karlsson, Y. C. Chao, and R. I. G. Uhrberg, *Surf. Sci.* **287/288**, 529 (1993).
- ¹¹⁴Y. Enta, S. Suzuki, and S. Kono, *Phys. Rev. Lett.* **65**, 2704 (1990).
- ¹¹⁵L. S. O. Johansson, R. I. G. Uhrberg, P. Mårtensson, and G. V. Hansson, *Phys. Rev. B* **42**, 1305 (1990).
- ¹¹⁶P. J. Feibelman, *Phys. Rev. Lett.* **34**, 1092 (1975).
- ¹¹⁷A. Zangwill and P. Soven, *Phys. Rev. A* **21**, 1561 (1980).
- ¹¹⁸H. J. Levinson and E. W. Plummer, *Phys. Rev. B* **24**, 628 (1981).
- ¹¹⁹A. Liebsch, *Phys. Rev. B* **36**, 7378 (1987).
- ¹²⁰D. Samuelsen, E. Pehlke, W. Schattke, O. Anderson, R. Manzke, and M. Skibowski, *Phys. Rev. Lett.* **68**, 522 (1992).
- ¹²¹A. Liebsch, *Electronic Excitations at Metal Surfaces* (Plenum, New York, 1997).
- ¹²²J. Ihm, D. H. Lee, J. D. Joannopoulos, and J. J. Xiong, *Phys. Rev. Lett.* **51**, 1872 (1983).
- ¹²³K. Yoo and H. H. Weitering, *Phys. Rev. Lett.* **87**, 026802 (2001).
- ¹²⁴H. Shigekawa, K. Hata, K. Miyake, M. Ishida, and S. Ozawa, *Phys. Rev. B* **55**, 15448 (1997).
- ¹²⁵K. Seino, W. G. Schmidt, and F. Bechstedt, *Phys. Rev. Lett.* **93**, 036101 (2004).